Chemical Engineering Journal 529 (2026) 172857

Contents lists available at ScienceDirect

Chemical Engineering Journal

journal homepage: www.elsevier.com/locate/cej

Gum Acacia-grafted multifunctional fluorescent hydrogel for ultra-trace sensing and sustainable recovery of samarium(III)

Somya Sadaf [a], Mrinmoy Karmakar [a], Yati Sharma [b], Anirban Mandal [b], Chinmay Ghoroi [a,*]

[a] *Department of Chemical Engineering, Indian Institute of Technology Gandhinagar, Gujarat, 382355, India*
[b] *Department of Chemistry, Indian Institute of Technology Gandhinagar, Gujarat, 382355, India*

ARTICLE INFO

Keywords:
Stimuli-responsive hydrogel
Sm(III)-sensing
Adsorptive recovery
Electrochemical and biomedical applications

ABSTRACT

Samarium (Sm) is an important rare earth element (REE) critical for permanent magnets, nuclear technologies, and advanced electronics. Limited accessibility and recent supply-chain disruptions associated with Sm have motivated efforts towards its recovery and reuse from waste streams. Existing approaches typically focus on either detection or recovery, thereby triggering the necessity for single reusable material serving as a platform for selective Sm(III) sensing, recovery, and post-adsorption applications. Herein, we report the design of a recyclable multifunctional gum acacia-grafted fluorescent copolymer hydrogel (GAFluoroCoP), which exhibits simultaneous selective sensing, efficient adsorption, and recovery of Sm(III) within a single framework. The GAFluoroCoP is synthesized via a one-pot strategy coupling 2-methylidenebutanedioic acid and methyleneacetic acid (synthetic) with naturally occurring gum acacia (GA), resulting in a material that exhibits self-healing, pH-responsive swelling, and moist adhesion properties. Importantly, GAFluoroCoP hydrogel displays intrinsic blue fluorescence with selective turn-off sensing of Sm(III) at ultra-trace concentrations (limit of detection = 37.5 pM), while simultaneously showing high adsorption capacity (127 mg g^{-1}), rapid uptake kinetics, and efficient desorption over five cycles, thereby demonstrating its reusability. Furthermore, the Sm-loaded GAFluoroCoP (SmGAFluoroCoP) exhibits semiconducting behavior (E_{gap} = 1.44 eV), electrochemical stability up to 500 bending cycles, and oxidative stress-mediated cytotoxicity, indicating potential electronic and biomedical applications. Collectively, this work establishes a closed-loop strategy for Sm management by integrating biopolymer-enabled fluorescence sensing, adsorption-enrichment, and sustainable recovery, thereby advancing environmentally compatible rare earth element recycling technologies.

1. Introduction

The growing dependence on rare earth elements (REEs) reflects their pivotal role in modern technologies, owing to their exceptional magnetic, luminescent, and mechanical properties [1]. These elements are fundamental to innovations in clean energy, electronics, and defense sectors, powering devices such as electric vehicles, wind turbines, high-performance batteries, lasers, and superconductors [1]. However, REEs occur in low natural concentrations and are unevenly distributed, with mining and extraction often limited to a few countries, most notably China, which currently controls the majority of the global supply [2,3]. This geographical imbalance, combined with the complex processing required to isolate REEs, has led to serious concerns about long-term availability. The situation is particularly pressing for critical REEs, like samarium (Sm), Dysprosium (Dy), and neodymium (Nd), whose demand increasingly exceeds supply [4,5].

Among these, samarium (Sm) holds particular importance due to its role in high-strength SmCo magnets, which are valued for their excellent thermal stability and resistance to demagnetization [6]. These magnets are essential in miniaturized electronics, aerospace, and green energy applications. Additionally, samarium holds nuclear relevance in the nuclear industry due to its stable 2+ and 3+ oxidation states, and its isotope Sm^{149}, which acts as a potent neutron absorber in control rods, thereby enhancing the safety of nuclear reactors [7]. Other uses include optical filter glass for lasers [8,9] microwave coatings [10] and capacitors [11]. Moreover, the Sm^{153} isotope has shown promise in cancer treatment due to its localized radiation delivery [12,13]. Recognizing its strategic value, the European Commission identified Sm(III) as a critical raw material for electronics and nuclear applications in 2010 [14]. Likewise, the U.S. Department of Energy classified Sm as a vital element

---

* Corresponding author.
E-mail address: chinmayg@iitgn.ac.in (C. Ghoroi).

https://doi.org/10.1016/j.cej.2026.172857
Received 24 September 2025; Received in revised form 5 January 2026; Accepted 9 January 2026

for defense, energy, and electronics sectors [15]. India has also prioritized Sm(III) under the Critical Minerals Mission, highlighting its role in clean energy, defense, and nuclear technologies [16]. As Sm is an important component in many electronic gadgets, end-of-life electronic articles represent a reliable source of Sm [17]. In fact, global e-waste generation currently reaches 50 million tons annually and is projected to rise to 74 million tons by 2030, representing a significant and valuable source of critical materials [18,19].

Industrial processes contribute to the release of samarium into the environment, where it bioaccumulates and disrupts the ecological balance, particularly in aquatic ecosystems [20,21]. Rare earth wastewater typically contains less than 50 ppm of REEs [22]. The extraction of one ton of ionic REE generates 150 to 250 m^3 of residual water, leading to resource depletion and the release of heavy metals, which severely impact ecosystems and biodiversity [23]. Studies have shown that administering Sm(III) at concentrations up to 500 μg/L for 8 days can cause bioaccumulation, oxidative stress, mitochondrial dysfunction, and lipidome alterations in marine mussels, highlighting potential environmental risks [24]. However, the biological function and toxicity of samarium remain less understood. In trout hepatocytes, Sm(III) exhibits significant toxicity by increasing metallothionein levels, indicating its role in oxidative stress [25]. In a recent study conducted on mice, exposure to 2000 mg L^{-1} of samarium resulted in a statistically significant increase in the apoptotic rate of testis cells, highlighting potential adverse effects on reproductive health at higher concentrations [26]. Soluble samarium salts are considered mildly toxic upon ingestion and may cause skin and eye irritation [27]. To date, no safety threshold value for samarium exposure in humans has been established. Depending on the compound, reported LD_{50} values for samarium range from 106 mg/kg to 343 mg/kg in animal studies [20]. In humans, exposure to samarium through inhalation or dermal contact can irritate the skin, eyes, and respiratory tract, emphasizing the need for stringent safety measures during handling and disposal [21,27]. These findings underscore the critical need for improved recovery, recycling and methods to minimize Sm(III) contamination and mitigate its associated health and environmental risks. However, prior to recovery, detection of trace levels of REEs, specifically Sm(III) in tailwater is equally critical.

Currently, Sm(III) detection relies on expensive and time-consuming techniques, such as atomic absorption spectrometry, inductively coupled plasma atomic emission spectroscopy, ion-selective electrode sensing [28], chromatography [29], optical sensing [30], and electrochemistry [31]. In contrast, fluorescence-based turn-off sensing of cations offers rapid, selective, and sensitive detection [32]. Jianjun et al. used fluorescence-based detection for Dy(III) using inorganic complexes, however the sensing material is sacrificial in the process [33]. Nevertheless, no current technology enables simultaneous detection of Sm(III) at ultra-low concentrations in tail water coupled with efficient recovery and reuse. To the best of our knowledge, no efficient, rapid, reusable, and highly selective sensor for Sm(III) detection and recovery has yet been reported.

Regarding the removal, common recovery methods include chemical precipitation [34], solvent extraction [35,36], biological processes [37], and adsorption [38–44]. Among these, adsorption is preferred due to its simplicity, cost-effectiveness, and reusability [45–48]. Natural adsorbents are affordable but often inefficient [45,47], whereas synthetic ones, although they perform better, lack biocompatibility [48,49]. Hadjittofi et al. reported that Sm(III) adsorption onto activated biochar exhibits a high adsorption capacity via carboxyl complexation, but suffers from slow kinetics and diffusion limitations at low pH [50]. Rasee et al. demonstrated that ligand-functionalized mesoporous silica composites exhibit excellent Sm(III) adsorption efficiency (155.13 mg g^{-1}) and strong selectivity; however, the process requires precise pH control (~5.0) to prevent hydroxide formation [51]. Therefore, there is a growing need for low-cost, sustainable adsorbents that are mechanically stable, biocompatible, and capable of selective and rapid Sm(III) adsorption with facile recovery.

Recently, scalable, reusable hybrid composites/gels have gained attention for sensing and removing hazardous components, including heavy and rare earth metals, dyes, and polyaromatics [52–57]. Multifunctional hydrogels, as flexible 3D polymer networks, are gaining significant attention for metal ion sensing [58,59] and removal, with swelling behavior governed by temperature, pH, and synthesis conditions [60,61]. Zhang et al. developed a ZIF-8@ALG composite hydrogel with enhanced mechanical stability and selectivity towards heavy REEs; however, strong complexation resulted in lower desorption efficiency [62]. Salem et al. prepared a PVA/PVP/PAAm terpolymer hydrogel via gamma irradiation, achieving improved mechanical strength, but high acrylamide content reduced gelation, and post-adsorption utilization was not addressed [63]. Wang et al. reported bifunctional alginate-based materials for simultaneous adsorption and sensing of Tb^{3+} and Eu^{3+}; however, mechanical properties were not evaluated, reusability was limited, and the adsorbent was discarded post-use [64].

Comprehensive studies on the mechanical properties of adsorbents remain largely unexplored, despite their critical importance for industrial applications. Fan et al. reported a CKNH-0.2 hydrogel with enhanced tensile strength and flexibility (strain >300%) achieved by incorporating kaolinite nanosheets; however, mechanical performance was highly sensitive to filler content, and compressive strength and long-term durability were not investigated [65]. Achieving an optimal balance between mechanical robustness and high adsorption capacity remains a significant challenge [66–68]. Moreover, detection and recovery of Sm(III) are generally reported separately, with minimal focus on simultaneous sensing and removal using a single material [69,70]. To the best of the authors' knowledge, no report currently exists on multifunctional hydrogels that integrate selective sensing and recovery of Sm(III), along with post-adsorption applications such as semiconducting behavior and tumor therapy.

Herein, we demonstrate the fabrication of an interpenetrating network hydrogel for selective Sm(III) sensing and recovery, along with its post-adsorption applications as a semiconducting material and in tumor therapy. We hypothesize that grafting naturally occurring gum acacia (GA) onto a synthetic polymeric backbone formed by polymerizing 2-methylidenebutanedioic acid (MDBDOA) and methyleneacetic acid (MEAA) yields a structurally robust, multifunctional hydrogel with intrinsic fluorescence. This design enables selective Sm(III) sensing, efficient adsorption–desorption, and post-recovery functionalities. The engineered hydrogel overcomes the poor mechanical strength and slow responsiveness of natural polysaccharide-based hydrogels while retaining GA biocompatibility.

The developed GAFluoroCoP exhibits intrinsic blue fluorescence that is significantly quenched by Sm(III), enabling selective sensing even in the presence of other REEs, with a limit of detection of 37.5 pM. The hydrogel also demonstrates rapid Sm(III) adsorption from unary, binary, and ternary mixtures, with a high adsorption capacity of 127 mg g^{-1} and efficient desorption over five cycles, confirming reusability. The high density of –COOH groups imparts pH-responsive behavior that facilitates both adsorption and desorption from industrial wastewater. Furthermore, Sm(III) uptake within the hydrogel microstructure improves its electrical behavior and triggers ROS-mediated cytotoxic effects, highlighting potential semiconducting and biomedical applications. Additionally, the oxidative stress–dependent toxicity of SmGAFluoroCoP is evaluated, and its anti-tumorigenesis potential is explored using MDCK cell lines. Overall, this study reports a one-pot synthesis of an intrinsically fluorescent hydrogel capable of selectively sensing Sm(III) down to picomolar levels and efficiently capturing it over multiple cycles. Furthermore, the semiconducting and anti-tumorigenesis properties of the post-adsorptive SmGAFluoroCoP hydrogel are demonstrated.

2. Materials and methods

2.1. Materials

The following chemicals were obtained from Sigma-Aldrich (high purity) and employed directly without additional purification: MEAA, MDBDOA, *N,N′*-methylenebisacrylamide (NNMBA), potassium persulfate ($K_2S_2O_8$), sodium bisulfite ($NaHSO_3$), dimethyl sulfoxide (DMSO), methanol (CH_3OH), and GA (molecular weight (MW) ~850 kDa). Metal salts, such as samarium(III) nitrate hexahydrate [$Sm(NO_3)_3{\cdot}6H_2O$, ≥99.9%], praseodymium(III) nitrate hexahydrate [$Pr(NO_3)_3{\cdot}6H_2O$, 99.9%], neodymium(III) nitrate hexahydrate [$Nd(NO_3)_3{\cdot}6H_2O$, 99.9%], cerium(III) nitrate hexahydrate [$Ce(NO_3)_3{\cdot}6H_2O$, ≥99.99%], europium (III) nitrate hydrate [$Eu(NO_3)_3{\cdot}5H_2O$, ≥99%], gadolinium(III) nitrate hexahydrate [$Gd(NO_3)_3{\cdot}6H_2O$, 99.9%], dysprosium(III) nitrate hydrate [$Dy(NO_3)_3{\cdot}xH_2O$, 99.9%], and ytterbium(III) nitrate pentahydrate [$Yb(NO_3)_3{\cdot}5H_2O$, 99.9%] were procured from Merck. Dimethyl sulfoxide-d_6 (DMSO-d_6), hydrogen peroxide solution (30% *w*/w in H_2O_2), 2,2-diphenyl-1-picrylhydrazyl (DPPH), and titanium(IV) oxysulfate ($TiOSO_4$) were procured from Sigma-Aldrich. Dulbecco's Modified Eagle Medium (DMEM), trypsin-EDTA, fetal bovine serum (FBS), and penicillin-streptomycin solution were supplied by Gibco (Thermo Fisher Scientific, USA). MTT (3-(4,5-dimethylthiazol-2-yl)-2,5-diphenyltetrazolium bromide) and MOWIOL were obtained from Merck.

2.2. Optimization and synthesis of GAFluoroCoP

GAFluoroCoP was prepared via free-radical solution polymerization, employing conditions optimized for both composition and temperature. The optimization process involved analyzing the equilibrium swelling ratio (ESR) of hydrogels synthesized using a response surface methodology (RSM) framework, which enabled evaluation of the combined influence of multiple parameters on ESR while reducing the overall number of experimental trials [66]. Since there were a total of six parameters that could be varied during GAFluoroCoP synthesis, a two-stage RSM design, consisting of Stage-I (Resolution-IV) and Stage-II Face-Centered Central Composite Design (FCCCD), was employed. In Stage-I, out of six parameters, such as molar ratio of MDBDOA:MEAA (*A*), temperature (*B*, °C), amounts of NNMBA (*C*, mg/mL), initiators (D, mg/mL), monomers (*E*, mg/mL), and GA (*F*, mg/mL)- three parameters possessing the maximum effect on ESR were identified. In the next stage, those three parameters were optimized by FCCCD by synthesizing thirteen hydrogels through software-generated compositions. The stress-strain analyses of these hydrogels were also performed to optimize mechanical stability of these hydrogels.

Under optimized conditions, MDBDOA (3.55 g) was neutralized to pH 5.5 using saturated aqueous NaOH, after which MEAA (1.45 g) and NNMBAm (0.5 g) were sequentially introduced. The reaction mixture volume was adjusted to 18 mL with deionized water and homogenized for 60 min. An aliquot of 800 μL was then withdrawn, and dried GA (1 mg incorporated into this portion, followed by ultrasonication for 10 min at room temperature to ensure uniform dispersion. Polymerization was subsequently triggered by introducing the initiator solution containing $K_2S_2O_8$ and $NaHSO_3$ (0.08 g each, dissolved in 200 μL deionized water). Gelation occurred rapidly at ambient conditions, requiring an inert N2 atmosphere. The resulting GAFluoroCoP was collected and purified by washing with a water/methanol mixture (1:3, *v*/v). Lyophilization of GAFluoroCoP was done to ensure complete drying. Finally, the dried GAFluoroCoP was crushed into a fine powder using a mortar and pestle for further utilization.

2.3. Structural elucidation

Structural elucidation of monomers, GA, NNMBA, GAFluoroCoP, and SmGAFluoroCoP was carried out by using proton nuclear magnetic resonance (^{1}H NMR) spectroscopy (Ascend NMR-500 MHz, Bruker) after dissolving/dispersing in DMSO-d_6 solvent. For FT-IR measurements, dried samples were analyzed using a PerkinElmer spectrometer equipped with an attenuated total reflectance (ATR) accessory, and spectra were recorded in the 400–4000 cm^{-1} range. The thermal behavior of dried GA, CoP and GAFluoroCoP was evaluated using thermogravimetric analysis (TGA) with a Netzsch Jupiter STA 449 F3 instrument, over the temperature range of 35–600 °C under a nitrogen atmosphere at a heating rate of 10 °C/min. The interaction and binding states of Sm(III) with GAFluoroCoP were further examined through X-ray photoelectron spectroscopy (XPS) using a K-Alpha+ system (Thermo Fisher Scientific, Waltham, MA, USA). The penetration of Sm(III) within the bulk of GAFluoroCoP was examined through XPS depth profile studies of SmGAFluoroCoP. The morphology of lyophilized CoP and GAFluoroCoP was examined using field emission scanning electron microscopy (FESEM, JEOL JSM 7600F, Japan), after coating the samples with a thin layer of platinum. Pore size distribution was analyzed using ImageJ software. For transmission electron microscopy (TEM), ultrathin film sections (<100 nm) were prepared by ultramicrotomy (Leica Ultracut EM FC6), mounted on copper grids, and imaged with a JEOL JEM 1400 instrument. Structural analysis of GA, GAFluoroCoP, and SmGAFluoroCoP was carried out using X-ray diffraction (XRD), with scans recorded over a 2θ range of 5–90° at a rate of 5° min^{-1}. Bio-atomic force microscopy (Bio-AFM) with a Bruker Nano Wizard Sense was employed to obtain detailed insights into the surface morphology. Confocal laser scanning microscopy (Leica TCS SP8) was used to investigate the cellular internalization of the developed formulations across different cell lines.

2.3.1. Rheological, mechanical, and physiochemical assessment of GAFluoroCoP

Rheological features of CoP and GAFluoroCoP samples were measured using a rheometer (MCR 302, Anton Paar GmbH, Graz, Austria). The storage modulus (G') and loss modulus (G'') were determined through strain and frequency sweep experiments. Strain was varied at 37 °C while maintaining a fixed frequency of 50 rad/s, and frequency was varied in the range of 1–100 rad/s while keeping the strain constant at 10%. All measurements were performed using a 25 mm parallel plate geometry with a 1 mm gap at 37 °C. Shear rate-dependent viscosity profiles of CoP and GAFluoroCoP were obtained across the shear rate range of 0.01–100 s^{-1}. The mechanical stability of the hydrogels was evaluated by tensile and compressive testing using a universal testing machine (Tinius Olsen, Norway). CoP and GAFluoroCoP specimens of uniform shape were equilibrated in deionized water for 30 min prior to testing under a load capacity of 10 kgf. For tensile stress measurements, samples of standardized dimensions (width: 5 mm, thickness: 3 mm, gauge length: 5 mm) were analyzed. Young's modulus was determined from the slope of the initial linear region of the stress–strain curve, ultimate strength from the maximum stress at the fracture point (FP), and toughness from the area under the stress–strain curve. Compressive strength was measured using cylindrical samples of uniform dimensions (height: 10 mm, diameter: 15 mm).

Shape adaptability of GAFluoroCoP was qualitatively assessed by spreading the hydrogel on a finger and bending it, while stretchability was quantified by manually elongating the hydrogel from its initial length (L_i, cm), which was gently pulled outward by hand until it broke (L_f, cm). The stretchability (%) was estimated by using Eq. 1.

$$\text{Stretchability}\ (\%) = \frac{L_f - L_i}{L_i} \times 100 \tag{1}$$

Similarly, GAFluoroCoP was subjected to twisting and rolling tests to evaluate its structural flexibility. Bending fatigue tests were also conducted to evaluate the mechanical durability of GAFluoroCoP. The hydrogel was subjected to 500 bending cycles at a 0–90° bending angle. Electrical performance was assessed by measuring the current–voltage (I—V) characteristics using a picoammeter across a voltage range of −6 V to +6 V. At last, the adhesive property of GAFluoroCoP towards different substrates was examined.

Swelling ratio (SR, %) was evaluated by immersing dried specimens (50 mg each of IPN and GAFluoroCoP, initial weight Wi) in 20 mL of phosphate-buffered saline (PBS, pH 7.4 and 8.5). Samples were withdrawn at predefined intervals (0.5, 1, 2, 4, 6, 12, 24, 48, and 72 h), gently blotted with tissue paper to remove surface-adhered liquid, weighed (Wf), and returned to the swelling medium. The swelling ratio (SR, %) was then calculated using the following Eq. 2 [67].

$$\mathrm{SR}\ (\%) = \frac{\mathrm{W_f} - \mathrm{W_i}}{\mathrm{W_i}} \times 100 \tag{2}$$

For determination of the equilibrium swelling ratio (ESR, %), hydrogel samples were immersed in deionized water (DW) until their weight stabilized, indicating attainment of equilibrium (We). The ESR was calculated using the following Eq. 3 [68].

$$\mathrm{ESR}\ (\%) = \frac{W_e - W_i}{W_i} \times 100 \tag{3}$$

Also, to determine the point of zero charge (pHPZC) of GAFluoroCoP, 0.2 g of the solid hydrogel was added to 25 mL of buffer solutions with varying initial pH values (pHi ~1–10) and stirred continuously at 200 rpm. After 72 h, the final pH (pHf) of each solution was recorded. The difference (ΔpH = pHf – pHi) was then plotted against pHi, and the pHPZC was identified as the pHi corresponding to zero ΔpH.

2.4. Sensing study of GAFluoroCoP

For spectroscopic characterization, GAFluoroCoP was dispersed in different solvents(DW, DMSO, and methanol), sonicated for uniform mixing, and centrifuged to separate the soluble fraction. The solubility was assessed by comparing the initial amount taken with the undissolved residue obtained after centrifugation. The resulting clear supernatants were subjected to UV–Vis absorption spectroscopy to identify the maximum absorption wavelength ($\lambda_{\max}$). Fluorescence emission spectra were then recorded on a Horiba Fluorolog-3 modular spectrofluorometer, using the respective λmax values as excitation wavelengths. To further understand solvent effects, binary mixtures of DW, DMSO, and methanol containing GAFluoroCoP were prepared and their emission responses were compared. Additionally, fluorescence quenching studies were performed by incrementally adding SmGAFluoroCoP solution to GAFluoroCoP, followed by recording changes in emission intensity.

2.5. Adsorption study of hydrogel systems

Adsorption Methodology: Isothermal adsorption experiments were conducted by dipping 0.015 g of dry GAFluoroCoP within 50 mL Sm (III) solution in the range of 5–50 mg L^{-1} at $\mathrm{pH_W} = 7$. Adsorption isotherm and kinetics data were determined by measuring unabsorbed Sm(III) concentrations (mg L^{-1}) at different time intervals by inductively coupled plasma mass spectrometry (ICP-MS). The equilibrium adsorption capacity (AC), q_{max}, (mg g^{-1}), rate constants, and thermodynamic parameters were estimated by methods reported [69,70]. Briefly, the equilibrium adsorption data were analyzed by fitting them to different isotherm models, including Langmuir, Freundlich, BET, Sips, and Henry models. (Eq. 4–8).

$$\text{Langmuir}: q_e = \frac{(q_{max} * K_L * C_e)}{(1 + K_L * C_e)} \tag{4}$$

$$\text{Freundlich Isotherm}: q_e = K_F C_e^{\left\{\frac{1}{n}\right\}} \tag{5}$$

$$\text{Linearized Langmuir}: \frac{1}{q_e} = \left(\frac{1}{q_{\max} * K_L * C_e}\right) + \left(\frac{1}{q_{max}}\right) \tag{6}$$

$$\text{Sips Isotherm}: q_e = \frac{(q_{max}\ (K_S * C_e)^n\ )}{(1 + (K_S * C_e)^n\ )} \tag{7}$$

$$\text{BET Isotherm}: q_e = \frac{(q_{BET} * K * C_e)}{((1 - K * C_e) * (1 + (K - 1) * C_e\ )\ )} \tag{8}$$

2.6. Post-Adsoptive study of hydrogel systems

2.6.1. Conductivity study of hydrogel systems

Electrical conductivity of SmGAFluoroCoP and GAFluoroCoP was evaluated using electrical impedance spectroscopy (EIS) with a three-electrode configuration on an electrochemical workstation (CHI660D, CH Instruments, Austin, TX, USA). Prior to measurement, hydrogel specimens were equilibrated in PBS (pH 7.4) for 30 min and then sandwiched between two indium tin oxide (ITO)-coated glass plates. The three-electrode system consisted of the hydrogel as the working electrode, a platinum wire as the counter electrode, and an Ag/AgCl electrode as the reference. Cyclic voltammetry (CV) was performed at scan rates of 10, 50, and 100 mV/s using the same setup, and the working potential of each hydrogel was determined from the CV plots. All experiments were conducted in triplicate to ensure reproducibility. The specific capacitance (*Cp*, in F g^{-1}) was derived from the cyclic voltammetry (CV) data using the Eq. 9 [71,72].

$$C_P = \frac{A}{2(V_2 - V_1)mk} \tag{9}$$

where *A* represents the area enclosed by the CV curve, V_2/V_1 are final/initial potentials (V), *m* is the mass of the electroactive hydrogel (g), and *k* is the scan rate (V s^{-1}). The onset potentials of oxidation and reduction observed in the CV curves were used to estimate the highest occupied molecular orbital (HOMO) and lowest unoccupied molecular orbital (LUMO) energy levels, from which the electronic bandgap of the hydrogels was calculated.

EIS was employed to measure the real (Z', Ω) and imaginary (Z'', Ω) components of impedance, the total impedance magnitude (Z_{mag}, Ω), the angular frequency (ω, Hz), and the phase angle (φ, dimensionless). These parameters were used to construct both Bode and Nyquist plots. By fitting the Nyquist plots, the solution resistance (R_s, Ω) was determined. This resistance value was then used to compute the electrical conductivity (σ, S m^{-1}) where *L* denotes the thickness of the glass slide (m) and *A* is its surface area (m^2) Eq. 10 [71].

$$(\sigma) = \frac{1}{R_S} \times \frac{L}{A} \tag{10}$$

2.6.2. In vitro radical generation tests

The H_2O_2-generating ability of the hydrogels was evaluated using a $TiOSO_4$-based assay. Briefly, a defined volume (0.3 mL, 2 mg/mL in deionized water) of GAFluoroCoP and SmGAFluoroCoP was enclosed within a dialysis membrane (MWCO: 12–14 kDa) and incubated at 37 °C in 5 mL of 1 mM H_2O_2 solution. At predetermined time points (6, 24, 48, and 72 h), 0.1 mL aliquots were withdrawn, mixed with 0.1 mL of 30 mM $TiOSO_4$ solution, and the absorbance was measured at 405 nm using a microplate reader. The hydroxyl radical (•OH) generation was assessed using a TMB assay. A fixed volume (0.3 mL, 2 mg/mL in deionized water) of Sm(III), GAFluoroCoP, and SmGAFluoroCoP was placed in a dialysis membrane (MWCO: 12–14 kDa) and incubated at 37 °C in 5 mL PBS. Aliquots (0.2 mL) were collected at 6, 24, 48, and 72 h, followed by the addition of 0.2 mL 0.03% H_2O_2 solution, 0.2 mL 30 mM $FeSO_4$, and 0.4 mL 1 mM TMB in DMSO, prepared in 0.5 M acetic acid buffer (pH 4.5). The mixture was incubated for 10 min, centrifuged at 13,200 rpm for 5 min, and the absorbance of the supernatant was recorded at 652 nm. The generation efficacy (%) of •OH was estimated by the following Eq. 11 [73]:

$$\text{Generation}\ (\%) = \left[1 - \left(\frac{A_1 - A_2}{A_0}\right)\right] \times 100 \tag{11}$$

Here, A_0, A_1, and A_2 represent absorbance values of control (DW instead of sample), samples, and background (DW instead of H_2O_2), respectively.

EPR spectroscopy was performed to further confirm •OH generation. H_2O_2 (10 mM, 0.2 mL) was combined with $FeSO_4$ (30 mM, 0.2 mL) in 0.5 M acetic acid buffer to produce •OH radicals. This solution (0.2 mL) was transferred into conical tubes containing GAFluoroCoP or SmGAFluoroCoP, followed by the addition of 0.5 mL of 5,5-Dimethyl-1-pyrroline-N-oxide (DMPO) solution (100 mM). The mixtures were incubated for 30 min at 37 °C, and the samples were analyzed using an EPR spectrometer (JES-X320, JEOL Ltd., Tokyo, Japan).

The cellular ROS-inducing ability of the hydrogels was examined in MDCK cells (ATCC CCL-34). Cells were seeded at 1 × 10^5 cells/well in a 12-well plate and cultured for 24 h. H_2O_2 (10 mM, 0.1 mL) was added and incubated for 6 h. Hydrogel samples (0.05 mL) were placed in polymer membrane inserts (12-well SPL Insert Hanging Tubes, SPL Life Sciences) and incubated with the cells for 72 h. After incubation, the media was removed, cells were washed twice with PBS (pH 7.4), and stained with 10 μM DCFH-DA for 20 min at 37 °C. Cells were resuspended in DPBS, and fluorescence imaging was performed using a Nikon Eclipse Ts2 microscope.

Cytotoxicity of GAFluoroCoP and SmGAFluoroCoP was evaluated using a live/dead viability assay. MDCK cells (1 × 10^5 cells/well) were cultured in a 12-well plate for 24 h, after that hydrogels (50 μL) were added via the polymer membrane insert system and incubated with cells for 72 h at 37 °C. Inserts were removed, cells were washed at least three times with DPBS (pH 7.4), and 1 mL of live/dead reagent (Thermo Fisher Scientific) was applied according to the manufacturer's instructions. After 30 min of incubation, dyes were removed, cells were washed, and fluorescence images were acquired using an inverted microscope (Nikon Eclipse Ts2), capturing calcein AM (green, live cells) and EthD-1 (red, dead cells).

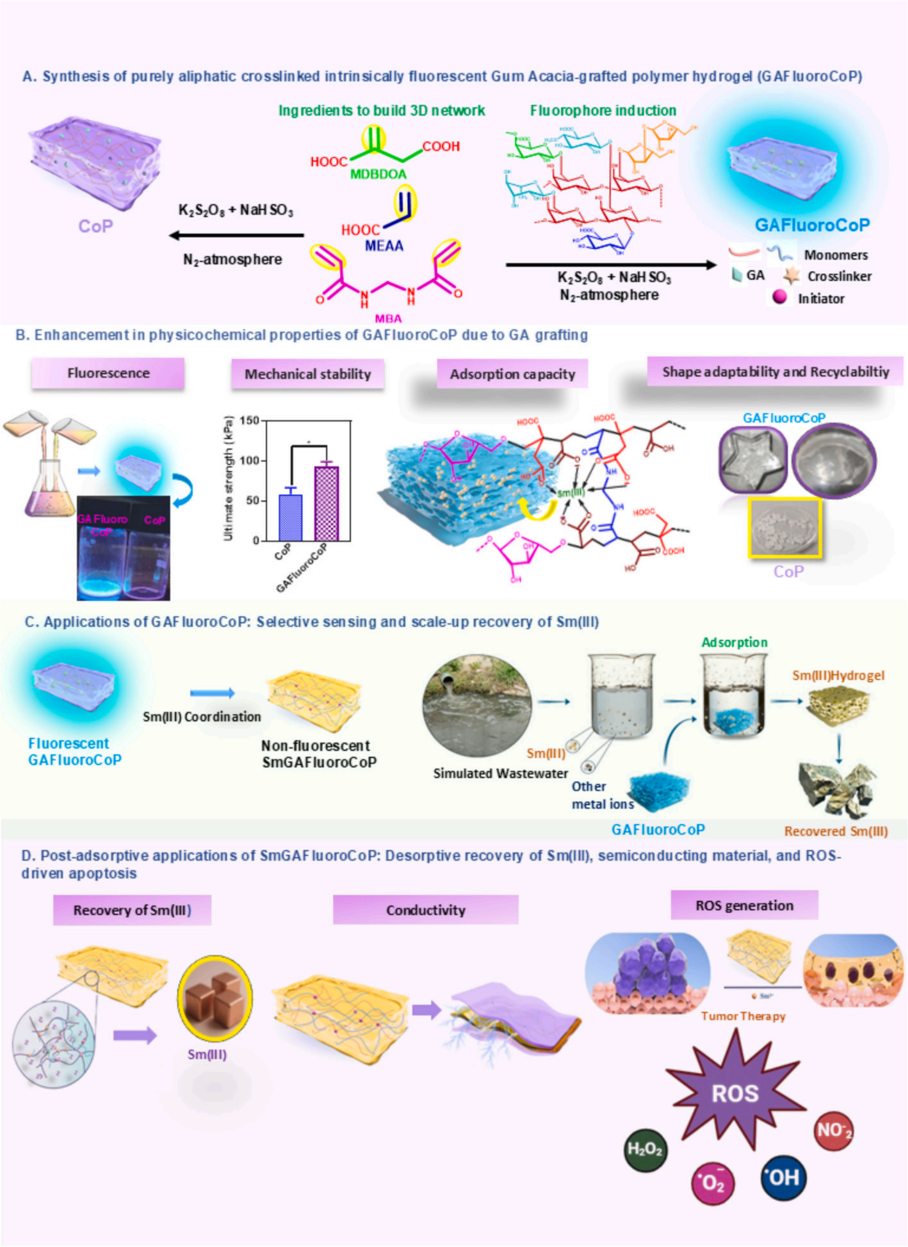

Fig. 1. Synthesis, characterization, application, and post-adsorptive application prospects of GAFluoroCoP.

2.7. Data analyses

Statistical analysis was carried out using ANOVA with post hoc test. Each experiment was repeated at least three times. Data are shown as the mean ± standard deviation (SD).

3. Results and discussion

3.1. Hydrogel framework design

Herein, the non-fluorescent monomers (MDBDOA and MEAA) were polymerized together in the presence of a non-fluorescent natural polysaccharide, GA, to obtain an intrinsically blue fluorescent hydrogel/ GAFluoroCoP (Fig. 1). The inclusion of GA not only introduced a fluorophore in Poly(MDBDOA-*co*-MEAA) (CoP), but also enhanced mechanical stability, shape adaptability, adhesiveness, adsorption capacity, complexation ability with terpsoitive REEs, adsorption-desorption recycling capacity, and electrical conductivity.

3.2. Statistical optimization of the synthetic parameters

To achieve the optimal balance between physicochemical parameters of hydrogel, *i.e,* mechanical properties and hydrophilic receptors (such as –OH, –COOH and $–COO^-$), optimization of the synthesis parameters is essential. This helps achieve the strong chelation with Sm (III), leading to its sensing and adsorption. The target of the as-reported GAFluoroCoP is to sense and adsorb Sm(III). According to the characterization data from FT-IR and XPS, the binding between GAFluoroCoP and Sm(III) was found to be predominantly chemical type involving the hydrophilic functionalities ($–COOH/ –COO^-$) of GAFluoroCoP. Therefore, from an application point-of-view, the maximum availability of these hydrophilic functionalities on GAFluoroCoP should be the basis for optimizing synthesis parameters. Since, swelling of a hydrogel typically depends on the population of hydrophilic functionalities embedded within it, quantification of hydrophilicity of a hydrogel via measuring its equilibrium swelling ratio (ESR) is logical. To achieve this, a two-stage Response Surface Methodology (RSM) optimization was adopted to find the perfect composition of synthesizing the highest-swelling hydrogel via performing the minimum number of experiments (Table S1). From Analysis of variance (ANOVA) data of first stage (Resolution-IV design) optimization, out of six major synthesis parameters studied, such as molar ratio of MDBDOA/MEAA (*A*, –); temperature (*B*, °C); and amounts of *N*,*N*′-methylene bisacrylamide (NNMBA, *C*, wt%), initiators (*D*, wt%), monomers (*E*, wt%), and GA (*F*, mg/mL), only *A*, *E*, and *F* parameters were found to cross the Bonferroni limit of 4.12236 (Fig. S1A and Table S2). Hence these three parameters were considered as the most significant terms and accounted for stage-II optimization, i.e., face-centered central composite design (FCCCD) (Tables S3 and S4). From FCCCD analysis, the optimized 3D response surface plots are obtained and displayed in Fig. S1B. Optimization of the synthesis parameters could be obtained from these 3D plots. After analyzing ANOVA generated using the ESR values of these new series of hydrogels as the input variables (Table S4), the optimum parameter values were found to be: 2.33, 18.61 wt%, and 2.65 mg mL^{-1} with a desirability of 0.955 (Fig. S2).

We then evaluated the mechanical properties of all fifteen hydrogels synthesized according to Table S4. Interestingly, H-15, having the maximum ESR, also exhibited the highest ultimate stress value of 38.84 ± 1.45 kPa (Fig. S3). Therefore, independent of the output parameters of optimization (ESR or mechanical stress), H-15 was found to be the best hydrogel.

3.3. Structural characterization of CoP and GAFluoroCoP

Elucidation of structures, associated bonding interactions, and grafting of GA in GAFluoroCoP have been carried out via ^1H NMR, FT-IR, XPS, EPR, TG, DTG, XRD, FE-SEM, HRTEM, and AFM analyses. From ^1H NMR (Fig. 2A), the C—C Coupled formation of polymer backbone could be inferred from the appearance of $–C\underline{H}_2–$ and $> C\underline{H}–$ peaks within 0.81–1.46 ppm and the simultaneous obsolescence of $\underline{H}_2C{=}C\underline{H}–$ peaks of MDBDOA, MEAA, and NNMBA within 5.78–6.35, 5.88–6.35, and 5.69–6.17 ppm (Figs. S4-S6), respectively. The inclusion of NNMBA in GAFluoroCoP could be inferred from the characteristics $–CON\underline{H}–$ and $–CONH–C\underline{H}_2–CONH–$ peaks within 8.12–8.46 and at 4.34 ppm, respectively. The ^1H NMR spectrum of GA (Fig. S7) validated a branched heteropolysaccharide architecture comprising *β*-D-galactopyranosyl backbones, *α*-L-arabinofuranose, *α*-L-rhamnopyranose, uronic acids, and their methylated derivatives [74]. The inclusion of GA within GAFluoroCoP could be understood from the appearance of small yet distinct peaks within 3.21–5.41 ppm. The grafting of GA via formation of $-CH_2 - O - CH_2-$ type ether moiety originating from the combination of $-CH_2OH$ of *α*-L-Ara*f* and $H_2C{=}CH–$ of CoP could be inferred from the notable shift of the characteristic $-CH_2OH$ peak of *α*-L-Ara*f* from 3.76 ppm in GmAc to 3.83 ppm in GAFluoroCoP.

From the FT-IR spectrum of GA (Fig. 2B and Table S5), the broad peak centered at 3299 cm^{-1} represented the extensive H-bonded O—H *str.* Occurring from the high population of hydrophilic –COOH functionalities. However, in CoP, comparatively sharper O—H *str.* Peak appeared at 3506 cm^{-1}, along with the appearance of a weak shoulder peak at 3236 cm^{-1} (Fig. 2B). The first peak indicated the presence of H-bonded O—H *str.*, whereas the second peak represented the non-H-bonded O—H *str.* Such observation indicated the presence of a lower extent of H-bonding in CoP due to the presence of hydrophobic polymer backbone. After grafting of GA in GAFluoroCoP, the H-bonding environment of CoP became broader (Fig. 2B), suggesting improvement of H-bonding attributed to the hydrophilic functionalities from GA. In GAFluoroCoP, the appearance of glycosidic bond-specific peak at 1037 cm^{-1} (this peak did not occur in CoP) indicated the incorporation of GA within the polymer matrix of GAFluoroCoP. The new appearance of peaks at 2945 and 1130 cm^{-1} in GAFluoroCoP supported the formation of $-CH_2 - O - CH_2-$ type ether moiety during grafting of GA within CoP moiety. Such $-CH_2 - O - CH_2-$ type moiety formation has been previously observed from ^1H NMR analysis.

Such $-CH_2 - O - CH_2-$ linkage during GA-grafting could also be inferred from the deconvoluted C 1 s spectrum of GAFluoroCoP (Fig. 3A) at binding energy (BE) = 286.15 eV due to $\underline{C}—O$ (sp^3). Besides, the deconvoluted C 1 s spectrum of GAFluoroCoP contained three more distinct peaks at 283.64, 284.65, and 285.37 eV because of $\underline{C}—\underline{C}$ (sp^3), $>\underline{C}{=}O$ (sp^2), and $–\underline{C}OO^-$ (sp^2), respectively. Therefore, from ^1H NMR, FT-IR, and XPS analyses, GA has been found to be grafted within CoP moiety through $-CH_2 - O - CH_2-$ type ether linkage.

To explore the thermal properties of the hydrogel specimens, TG analyses of GA, CoP, and GAFluoroCoP were studied (Figs. S8A and 3C). For GA, a three-stage degradation pathway could be observed, viz. (a) the initial phase (up to 150 °C) indicated moisture loss (~ 10.9%), (b) second phase (200–300 °C) demonstrated volatilization of smaller fragments (~ 6.03%), and (c) third decomposition phase (300–400 °C) clarified decomposition of the polysaccharide backbone (~53.77%) [74,75]. The thermogram of CoP contained three major decomposition stages, representing evaporation of physically and/or chemically bonded water molecules; anhydride formation and its decomposition; and finally the dissociation of the polymer backbone. Grafting of GA significantly improved the thermostability of all the stages, of which the delayed decomposition in the first stage was associated with the extensive H-bonding due to GA-grafting, and the second stage thermostability was due to the formation of covalent bonds during grafting. In the second stage of decomposition of CoP and GAFluoroCoP, the appearance of two distinct DTG peaks at 342/ 425 and 342/ 412 °C (Fig. 3D), respectively, justifies the co-occurrence of two phenomena, i.e., acid-to-anhydride formation and followed by anhydride decomposition [74].

The Fig. 4A shows the FE-SEM images and morphological analysis of

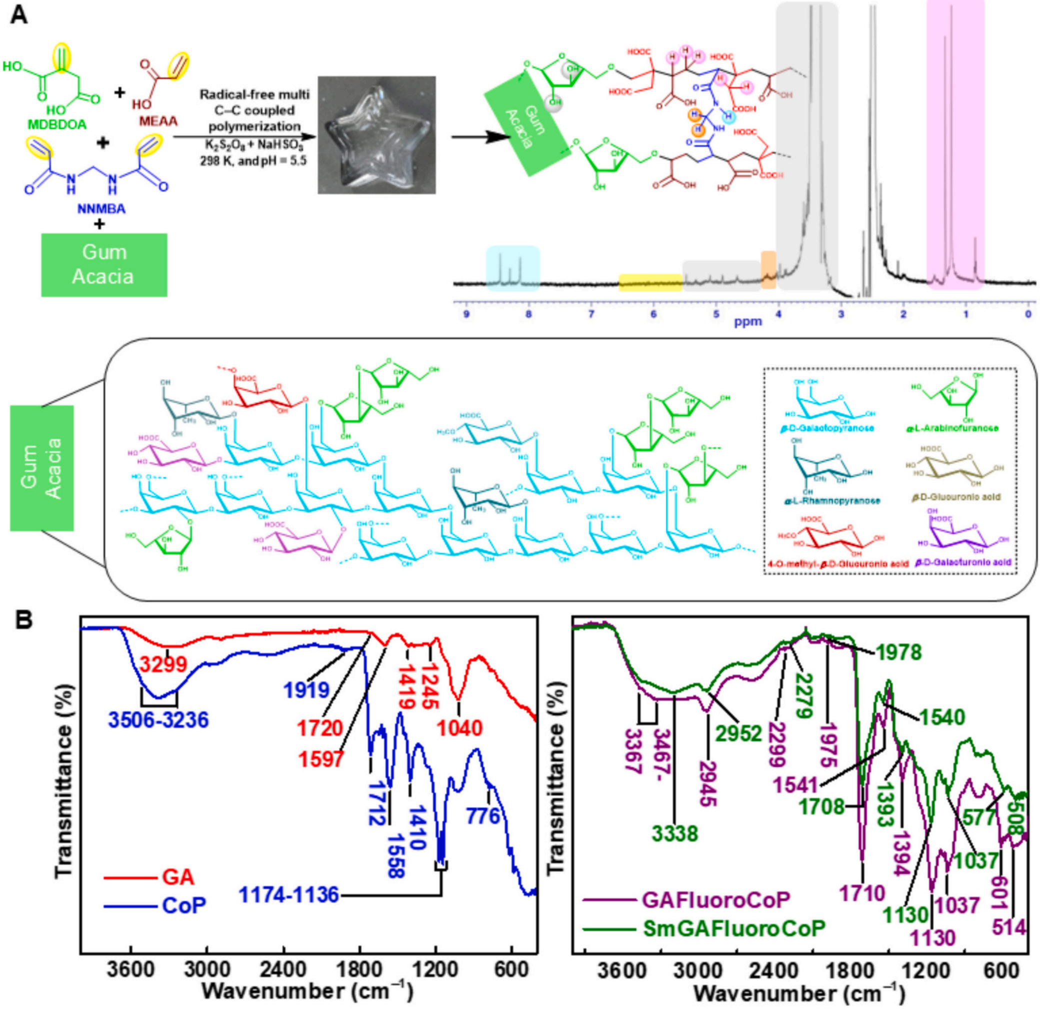

Fig. 2. Structural elucidation of GAFluoroCoP: (A) Synthetic sketch of GAFluoroCoP from reactants and optical image and ^{1}H NMR spectrum of GAFluoroCoP. (B) FT-IR of GA, CoP, GAFluoroCoP, and SmGAFluoroCoP.

fridge-dried GAFluoroCoP. The porous surface properties of GAFluoroCoP could be observed from Fig. 4A. For GA, the XRD profile showed a broad hump at $2\theta = 18.7^0$ and a weaker feature near 42.3^0 (Fig. S8B), consistent with amorphous polysaccharides lacking long-range crystalline order. This disordered arrangement contributes to GA's high solubility and functional versatility [74,75]. From XRD spectrum of GAFluoroCoP (Fig. S9), two medium intensity peaks were observed at $2\theta = 10.25$ and 23.34^0 due to H-bonding based orderley arrangement of Miller indices and covalently bonded polymer matrix, respectively. Fig. 4B shows the HRTEM image of GAFluoroCoP. The distinct particulate grains of nano-dimension is observed. AFM analysis (Fig. 4C) reveals that the CoP exhibited spherical morphology with an average diameter of ~220 nm, as supported by the size distribution. In contrast, GAFluoroCoP showed increased particle size (Fig. 4D). The average particle diameter notably increased, as quantified in Fig. 4C and D. This size enhancement can be attributed to higher crosslinking density and molecular entanglement arising from the GA grafting, leading to more compact and aggregated structures [76–78].

3.4. Structural characterization of SmGAFluoroCoP and establishment of adsorption mechanism

Interaction of Sm(III) brought about significant changes in the microstructures of GAFluoroCoP that help us to identify the interaction pattern of Sm(III) with GAFluoroCoP. From FT-IR (Fig. 2B), the H-bonding was found to be broadened after Sm(III)-adsorption because the adsorption was carried out at $pH > pH_{PZC}$. Importantly, the shifting of >C=O *str.* of –COOH, >C=O *asym. Str.* of $–COO^-$, and > C=O *sym. Str.* of $–COO^-$ from 1720, 1561, and 1414 cm^{-1} of GAFluoroCoP to 1708, 1540, and 1394 cm^{-1} in SmGAFluoroCoP suggested the chemical interaction between Sm(III) and $–COO^-$ of GAFluoroCoP during sensing and adsorption. Moreover, the appearance of small yet distinct peaks within 418–613 cm^{-1} in SmGAFluoroCoP supported the formation of Sm—O type bonding. Again, the insignificant alteration of glycosidic and grafting-associated $–CH_2–O–CH_2–$ peak after Sm(III)-loading indicated the non-involvement of glycosidic and ether linkages in binding with Sm(III).

To further explore the type of chemical attachment involved during the adsorption of Sm(III) by $–COO^-$ of GAFluoroCoP, multi-nuclear XPS data has been analyzed. The distinct peak at BE of 1085 eV (Fig. 3A and Table S6) at the wide-angle survey scan of SmGAFluoroCoP confirmed the presence of Sm(III) in SmGAFluoroCoP. Furthermore, the shifting of O 1 s peaks of $>C=\underline{O}$, $–C\underline{OO}^-$, and $–C\underline{O}OH$ from 531.08, 532.16, and 535.25 eV of GAFluoroCoP to 531.95 (+0.87), 533.23 (+1.07), and 536.02 (+0.77) eV in SmGAFluoroCoP inferred the occurrence of coordinate bonding between Sm(III) and $–COO^-$/ –COOH of GAFluoroCoP. Such coordination could also be supported from the appearance of Sm $3d_{5/2}$ and Sm $3d_{3/2}$ peaks at BE = 1083.14 and 1110.74 eV, respectively, which are significantly lower than those of 1084.50 and 1111.60 eV, respectively, from the pristine Sm(III)-compounds [79].

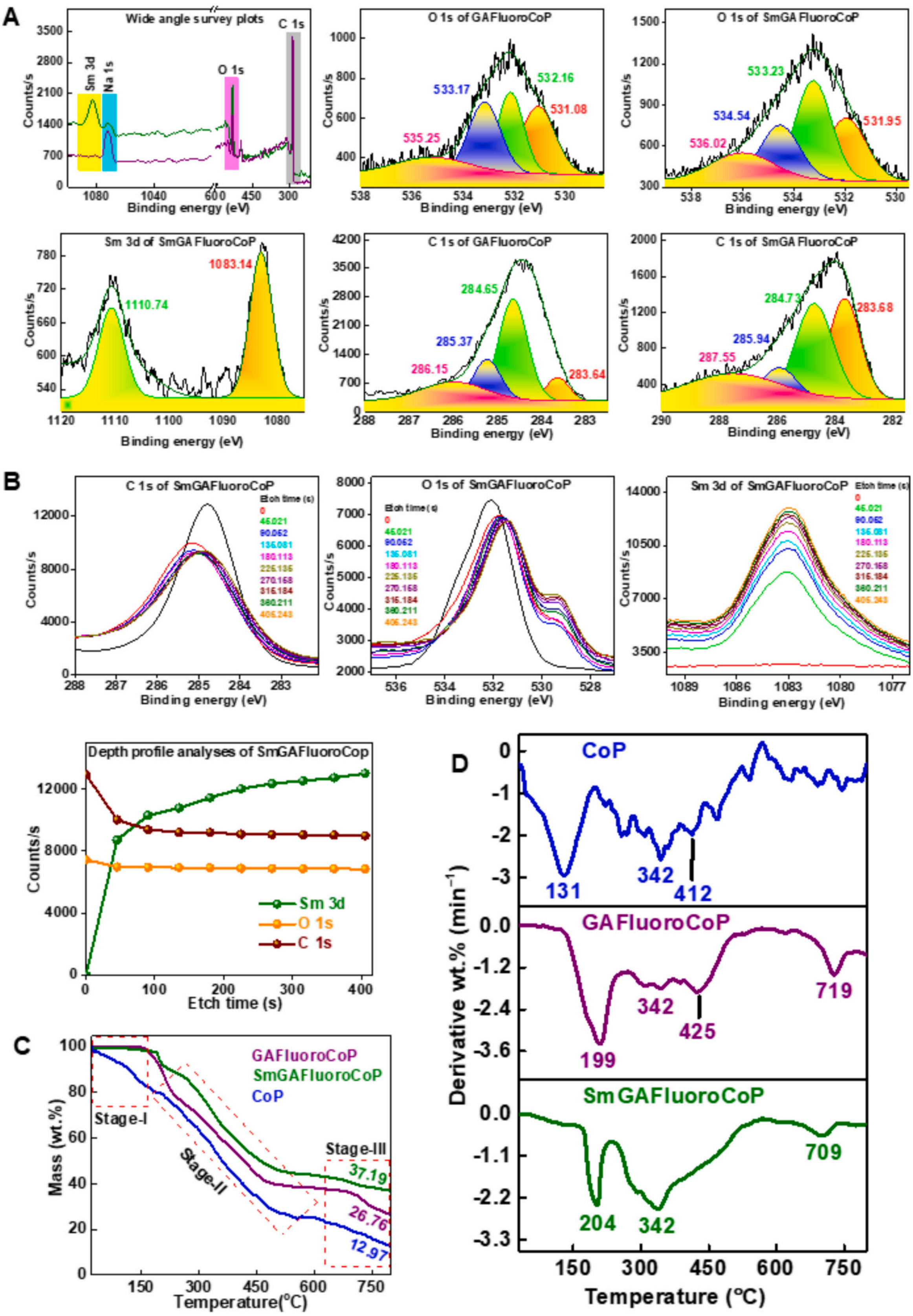

Fig. 3. Structural elucidation of GAFluoroCoP: (A) XPS profiles (wide angle survey scans and narrow scan fitting) of GAFluoroCoP and SmGAFluoroCoP. (B) XPS depth profile studies of SmGAFluoroCoP. (C/D) TG/DTG analyses of CoP, GAFluoroCoP, and SmGAFluoroCoP.

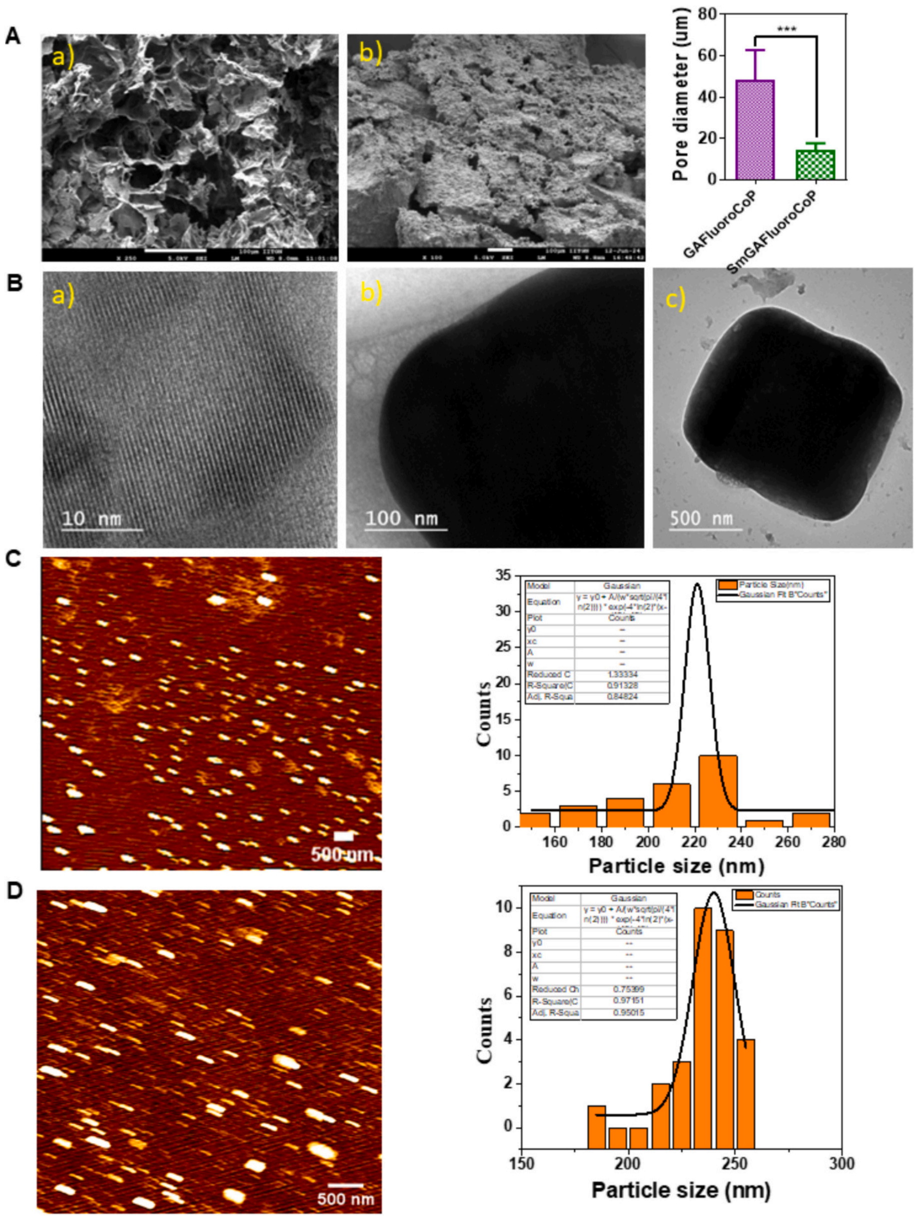

Fig. 4. Microscopic studies of GAFluoroCoP and SmGAFluoroCoP: (A) FE-SEM images and the corresponding pore diameter values of GAFluoroCoP and SmGAFluoroCoP (Scale bar: 100 μm). (B) TEM images of (a) GAFluoroCoP and (b-c) SmGAFluoroCoP at 10 and 100/500 nm scale bars, respectively. (C/D) AFM images of CoP (scale bar: 500 μm)/GAFluoroCoP (scale bar: 500 nm) and the corresponding size distribution histogram fitted with a Gaussian curve.

In SmGAFluoroCoP (Fig. 3C), the initial lower thermostability up to 150 °C was associated with the poor H-bonding, because adsorption was carried out at pH > pH_{PZC}, where most of the –COOH were converted to $–COO^-$. However, the recovery of thermostability of SmGAFluoroCoP in the second stage could be linked with the formation of $–COO^- \rightarrow$ Sm(III) coordinate bonds, which prevent the dissociation of acid moieties into the corresponding anhydrides. Finally, the availability of 37.19 wt% residue in SmGAFluoroCoP compared to 26.76 wt% residue of GAFluoroCoP inferred the presence of thermostable inorganic Sm(III) ions. In DTG of SmGAFluoroCoP (Fig. 3D), the anhydride decomposition peak could not be located, suggesting the inhibition of anhydride decomposition due to $–COO^- \rightarrow$ Sm(III) coordinate bonds [79].

From FE-SEM image of fridge-dried SmGAFluoroCoP (Fig. 4A), the porous nature of GAFluoroCoP could not be visualized for SmGAFluoroCoP. These observations might indicate the surface coverage of GAFluoroCoP by Sm(III). From the EDS diagram (Fig. S10), 66.5 atom% of Sm(III) coverage inferred the attachment of Sm(III) onto GAFluoroCoP.

To examine whether the population of Sm(III) was predominantly on the surface or penetrated deep into the pores of GAFluoroCoP, we studied XRD analyses of SmGAFluoroCoP. From Fig. S9, no Sm(III)-specific sharp peak could be observed in SmGAFluoroCoP and the peak at $2\theta = 23.34^0$ in GAFluoroCoP turned into a shoulder peak in SmGAFluoroCoP, indicating penetration of Sm(III) within the bulk of GAFluoroCoP.

To justify the occupation of Sm(III) onto the surface or within the bulk of GAFluoroCoP, XPS depth profile experiment of SmGAFluoroCoP were studied (Fig. 3B). The intensity of Sm $3d_{5/2}$ orbital was found to be zero at the etch time = 0 s, suggesting negligible population of Sm(III) onto the surface of GAFluoroCoP. However, the population of Sm(III) was found to increase with the increase in etch time, suggesting deeper penetration of Sm(III) within the bulk of GAFluoroCoP. Therefore, it could be inferred that most of the harvested Sm(III) penetrated within the bulk of GAFluoroCoP. Therefore, from the above discussions, it can be concluded that Sm(III) was adsorbed onto GAFluoroCoP through chemical attachment involving –COO^- of GAFluoroCoP.

3.5. Physicochemical and rheological properties of CoP and GAFluoroCoP

To evaluate the gelation behavior of the synthesized GAFluoroCoP hydrogel, inversion tests and rheological analyses are performed (Fig. 5A). From the inversion test, the successful sol-to-gel transition could be achieved after simple mixing of monomers, crosslinker, and initiator solutions at room temperature, without applying any external temperature, pressure, and inert atmospheric conditions (i.e., N_2). Notably, gelation was achieved across a wide temperature range (273–323 K), demonstrating the robustness and adaptability of this synthesis process under globally ambient conditions. The equilibrium swelling ratio (ESR) values remained consistent across this temperature range (Fig. S11), further validating the universal applicability of the synthesis method.

Rheological features of these hydrogel samples were measured with a rheometer (Figs. 5A and S12). From the frequency sweep measurements of CoP and GAFluoroCoP, the storage moduli (G') were found to be higher than those of loss moduli (G''), which ensured the predominant gelation properties. However, for CoP, the higher G' over G'' value was observed only up to 18% strain, whereas for GAFluoroCoP, the $G' > G''$ was maintained up to 30% strain. These data showed that there was an increase in the structural robustness of GAFluoroCoP compared to CoP under increasing deformation. Similarly, from the frequency sweep, the $G' > G''$ values were observed up to 3 and 100 rad/s for CoP and GAFluoroCoP, respectively. Additionally, the maximum G' values of CoP and GAFluoroCoP were found to be 416 and 1488 kPa, respectively, at 100 rad/s frequency, which clearly indicated the improvement in gelation strength of CoP after GA-grafting. Such strong improvement of rheological properties in GAFluoroCoP over CoP indicated the formation of strong chemical bonds between CoP matrix and GA during GA-grafting. From the viscosity sweep test, GAFluoroCoP was found to demonstrate the pronounced shear-thinning behavior, with viscosity continuously decreasing as the shear rate increased from 0.1 to 100 s^{-1}. This non-Newtonian response suggested that while the internal network resists flow under low shear, it progressively breaks down under higher shear conditions, facilitating easier deformation [80].

The structural flexibility of GAFluoroCoP was examined through rolling, twisting, stretching, bending, and shape adaptability experiments. In the moist state, GAFluoroCoP exhibited excellent results in these experiments (Fig. 5B) that confirmed the flexibility of the GAFluoroCoP matrix. Moreover, during the stretchability experiment, the degree of stretching of GAFluoroCoP appeared to be 0.8, which again confirmed its superior structural flexibility. In this context, it is important to mention that CoP did not respond to any of the above-mentioned experiments, confirming the mechanical fragility of its structure.

Another important property of GAFluoroCoP is its self-healing ability. According to Fig. 5B, the two pieces of GAFluoroCoP could be joined after placing the freshly cut fragments close to each other. We investigated the rheology of self-healing by measuring G' values of GAFluoroCoP at different strains. The rapid attainment of the maximum G' value after increasing the strain from 1% to 100% signified the superior self-healing property. Such self-healing property is essential because it helps in maintaining the structure of GAFluoroCoP during continuous flow of wastewater even at high velocity.

Mechanical stability ensures the structural robustness of hydrogels suitable for delivering high-performance for a longer time and also enables recycling uses for multiple cycles. The tensile and compressive stress values of CoP and GAFluoroCoP were measured to assess their mechanical properties (Fig. 5C). The tensile stress vs. strain curves for all samples displayed three distinct regions: an initial elastic zone extending up to the yield point (YP), followed by a characteristic J-shaped strain-stiffening region, where the slope increased with strain up to the breaking stress (BS), and finally, a post-BS region where the slope decreased until the fracture point (FP), leading to complete failure of the hydrogel network [81]. The ultimate tensile strength of CoP and GAFluoroCoP are found to be 65 ± 4 kPa and 93 ± 4 MPa, respectively, which are significantly higher than those reported for acrylic-based copolymers [81,82]. Again, from the compressibility stress plot, the attainment of the higher compressibility (1.12 MPa) at higher strain (65%) for GAFluoroCoP compared to lower compressibility (0.92 MPa) at lower strain (48%) of CoP inferred the structural toughness attained by GA-grafting within CoP. Toughness and Young's moduli of CoP and GAFluoroCoP were also calculated from tensile stress vs. strain curves. GAFluoroCoP possessed higher toughness and Young's modulus compared to CoP.

We then investigated the adhesiveness of GAFluoroCoP with different materials, such as glass, steel, and polystyrene, in both dry and moist states. From Fig. 5D, the excellent attachment of moist GAFluoroCoP with all these materials confirmed its strong adhesion in the moist state. However, dry GAFluoroCoP did not attach to any of the above-mentioned substances, which indicated the involvement of water molecules in creating the adhesive force to GAFluoroCoP. Such strong adhesion in the hydrated state is very helpful in installing GAFluoroCoP at different portions of the pipelines carrying industrial wastewater (Fig. S13).

Next, we studied the swelling-deswelling behavior of GAFluoroCoP at different pH. From Figs. S14 and S15, the swelling ratios (SRs) of both CoP and GAFluoroCoP were found to increase significantly from pH ~ 2 to 7, followed by an insignificant increase beyond pH ~8. The probable reason behind the increase in SR with increasing pH could be the higher population of –COO^-, compared to –COOH at the higher pH solutions. The pH_{PZC} of CoP and GAFluoroCoP are 5.09 and 5.22, respectively (Fig. S16). Therefore, at pH higher than those of 5.06 and 5.18, the surfaces of CoP and GAFluoroCoP are predominantly anionic, i.e., –COO^-. These –COO^- groups repel each other to create voids, where water molecules can be entrapped. However, –COOH groups tend to pull the polymer chains close to each other via H-bonding. Therefore, deprotonation of –COOH to –COO^- was responsible for the higher SR [83]. However, at very high pH, the presence of excess amounts of counter ions made swelling less [83]. Therefore, the optimum pH was found to be ~7. Fig. 5E shows the optical images of swelled/deswelled GAFluoroCoP at different pH. Moreover, the significantly higher SR and ESR values of GAFluoroCoP compared to CoP could be ascribed to the hydrophilic functionalities provided by GA. Herein, swelling represents attractive forces within $H^{\delta+}$ of H_2O and –COO^- of CoP/GAFluoroCoP. Therefore, higher swelling is expected to replicate the attraction between M^{n+} and –COO^- of CoP/GAFluoroCoP, and hence, GAFluoroCoP with higher swelling should possess a higher adsorption capacity (AC) towards cations compared to CoP.

The kinetics of polymerization was monitored by observing the increase in particle size through live microscopic imaging. After initiating the polymerization reaction, the increase in particle size could be observed up to 50 s (Fig. 5F), and after that, the particle size became almost constant. This observation suggested the attainment of polymerization in ~50 s. Such rapid polymerization is beneficial for commercial uses. Moreover, the maximum particle size was found to be 480 ± 25 nm, which confirmed the nano-dimension of GAFluoroCoP.

3.6. Fluorescence studies of GAFluoroCoP

The fluorescence activities of ingredients, i.e., MDBDOA, MEAA, NNMBA, and GA; CoP; and GAFluoroCoP were investigated to obtain information about the probable origin of the fluorophore. From Fig. 6A, monomers, NNMBA, and CoP were observed to be non-fluorescent, whereas GAFluoroCoP exhibited brilliant blue fluorescence in both solid and solution phases. Since GAFluoroCoP possessed the optimum balance between hydrophilicity and hydrophobicity, we checked its fluorescence activity in three solvents of different polarities, i.e., DW,

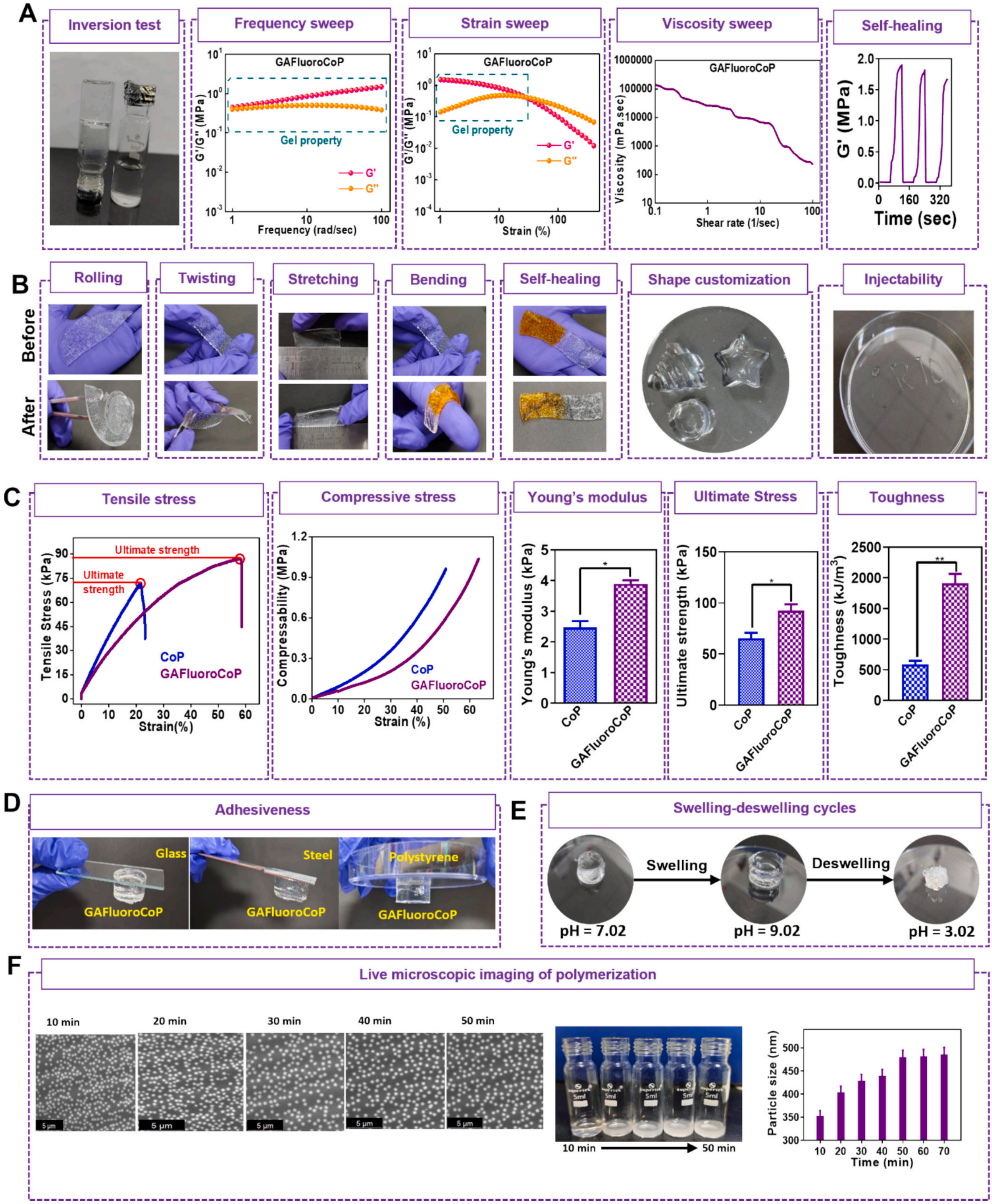

Fig. 5. Physicochemical properties of hydrogel systems: (A) Inversion test and rheological analyses of GAFluoroCoP. (B) Demonstration of structural integrity, shape adaptability, and injectability of GAFluoroCoP. (C) Mechanical properties of CoP and GAFluoroCoP. (D) Adhesion property of GAFluoroCoP with respect to different substrates. (E) Swelling and deswelling images of GAFluoroCoP. (F) Live gelation microscopic study of GAFluoroCoP at different time intervals. Data are presented as mean ± SD ($n = 3$). Statistical significance was determined using one-way ANOVA followed by Tukey's post hoc test. $^{*}p < 0.05$ between indicated groups.

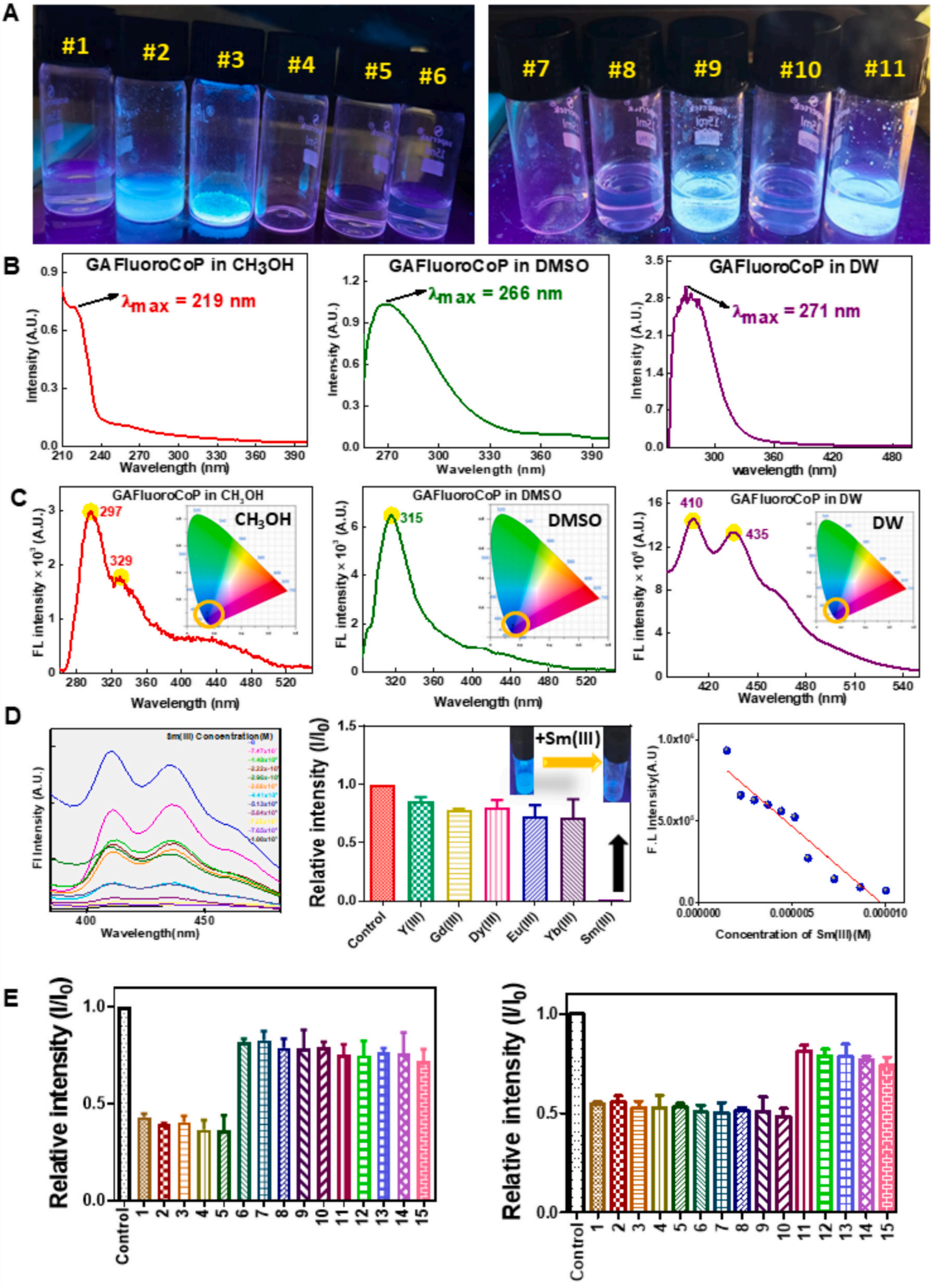

Fig. 6. Fluorescence studies: (A) Optical fluorescence images of CoP (#1), GAFluoroCoP in solution phase (#2), GAFluoroCoP in solid state (#3), blank vial (control/#4), MEAA (#5), MDBDOA (#6), control (#7), CoP in CH3OH (#8), GAFluoroCoP in CH3OH (#9), CoP in DMSO (#10) and GAFluoroCoP in DMSO (#11). (B) UV–vis spectra GAFluoroCoP in $CHCl_3$, DMSO, and DW. (C) Fluorescence emission spectra of GAFluoroCoP in $CHCl_3$, DMSO, and DW (Insets show the corresponding CIE chromaticity plots). (D) Turn-off sensing of GAFluoroCoP with the increased addition of Sm(III), I/I_0 plots of GAFluoroCoP in presence of various rare earth element's binary mixtures, and limit of detection (LOD) plot. (E) Fluorescence quenching (turn-off sensing) behavior of GAFluoroCoP upon interaction with binary metal ions, along with I/I_0 plots illustrating its response.

CH_3OH, and DMSO. GAFluoroCoP was found to be blue fluorescent even in CH_3OH and DMSO solutions (Fig. 6A), suggesting the polarity-independent fluorescence of GAFluoroCoP. Therefore, we refer to the fluorescence of GAFluoroCoP as an intrinsic property. However, to obtain excitation wavelengths of GAFluoroCop in these three solvents, first we studied the UV–vis spectra of GAFluoroCop after dissolving it into DW, CH_3OH, and DMSO. From Fig. 6B, the λ_{max} values were found to be 219, 266, and 271 nm for CH_3OH, DMSO, and DW, respectively. Such bathochromic shift of λ_{max} values with the increase in solvent polarity has been reported in the literature [84]. Therefore, the fluorescence emission experiments were carried out by considering excitation wavelengths at 219, 266, and 271 nm for CH_3OH, DMSO, and DW, respectively. The emission plots of GAFluoroCoP in different solvents are presented in Fig. 6C, in which the maxima values appear at 297/329, 315, and 410/435 nm in CH_3OH, DMSO, and DW, respectively. The type of color generated from such emission maxima could be predicted from CIE 1931 plots. Herein, all three CIE 1931 plots (insets of Fig. 6C) predict the occurrence of blue coloration. The maximum intensity of fluorescence emission in DW may be ascribed to the better solubility of GAFluoroCoP in DW. Therefore, all other fluorescence data were collected in DW medium. Notably, grafting of the non-fluorescent GA within the matrix of non-fluorescent CoP generated the intrinsic clue fluorescence in GAFluoroCoP, suggesting the probable extended electronic transfer within the H-bonding-driven fluorescence emission in GAFluoroCoP matrix [85,86].

To gain a deeper insight into the fluorescence mechanism, both the ground state (GS) and excited state (ES) electronic structures were subsequently examined using ORCA with the Becke, 3-parameter, Lee-Yang-Parr (B3LYP) exchange–correlation functional and the def2-split valence polarization (SVP) basis set (Fig. S17). The frontier molecular orbitals in the ground state revealed a clear spatial separation between Highest Occupied Molecular Orbital (HOMO) and Lowest Unoccupied Molecular Orbital (LUMO), with negligible overlap, indicating a charge transfer-driven process. The ES orbital optimization further yielded the energies of five low-lying states, viz. S_1, S_2, S_3, S_4, and S_5, at 0.681, 0.751, 0.785, 1.078, and 1.158 eV, respectively. The particularly low energy of S_1 aligned with the GS orbital distribution and reinforced the charge transfer character of the excitation. Therefore, the GS and ES analyses indicated the primary occurrance of charge transfer mechanism as the basis of fluorescence in GAFluoroCoP.

3.7. *GAFluoroCoP as a fluorescent probe for selective Sm(III) sensing*

The UV–Vis images of Sm(III) solutions prepared in deionized water (DW), methanol (CH_3OH), and dimethyl sulfoxide (DMSO) confirmed that Sm(III) is non-fluorescent, demonstrating the absence of intrinsic fluorescence in these solvents (Fig. S18). We then investigated the effects of adding metal ion solutions on the fluorescence intensity of GAFluoroCoP (Fig. 6D). With the continuous addition of Sm(III) solution, the fluorescence intensity of GAFluoroCoP decreased gradually, suggesting the possible alteration in the transition orbitals of GAFluoroCoP due to complexing with Sm(III)-ions. The possible coordinate bonding-based complexation of Sm(III) with GAFluoroCoP via formation of $-COO^- \rightarrow$ Sm(III) has already been established earlier from FT-IR and XPS analyses. Importantly, upon addition of other solutions of REMs, i.e., Y(III), Gd(III), dy(III), Eu(III), and Yb(III), no such quenching of fluorescence intensity could be observed. Despite having no intrinsic fluorescence property, Sm(III) could quench the overall fluorescence of GAFluoroCoP, indicating the quenching mechanism was not merely due to on Sm(III)-deposition on GAFluoroCoP, the strong chemical interaction of GAFluoroCoP with Sm(III) was the reason behind the fluorescence quenching. We then calculated the relative fluorescence intensity (I/I_0) values by dividing the fluorescence intensities of 0.1 mM REE-GAFluoroCoP solutions by the fluorescence intensity of 0.1 mM GAFluoroCoP solution (designated as control). The I/I_0 plot of all the REEs (added as unary method) has been depicted in Fig. 6D. The unusually low I/I_0 of SmGAFluoroCoP compared to the other REE-adsorbed GAFluoroCoP inferred the selectivity of GAFluoroCoP towards sensing Sm(III). The inset photograph of Fig. 6D depicted the visual observation of fluorescence quenching of GAFluoroCoP after the addition of Sm(III) solution. We then calculated the LOD value of Sm(III) detection, and it was 37.5 picoM (Fig. 6D). We then evaluated the Time-Correlated Single Photon Counting (TCSPC) experiments of GAFluoroCoP and SmGAFluoroCoP to infer the fluorescence quenching. The significant decrease in the $< t >$ value from 1.2397 ns of GAFluoroCoP to 0.2719 ns in SmGAFluoroCoP (Fig. S19) indicated the quenching of the intrinsic blue fluorescence of GAFluoroCoP after sm(III)-addition.

The selective sensing of Sm(III) by GAFluoroCoP was also tested in the presence of one and two REMs, designated herein as binary and ternary fluorescence experiments, respectively (Fig. 6E and Table S7). These data clearly indicated the quenching of fluorescence intensity of GAFluoroCoP in the presence of only Sm(III). Overall, GAFluoroCoP can sense Sm(III) individually or in-presence of one or two other metal ions.

We then utilized EDTA-based complexation experiments to confirm the complexation of Sm(III) with GAFluoroCoP as the basis of fluorescence quenching (Fig. S20). EDTA solution does not contain any fluorescence properties at 412 and 435 nm, which is the $\lambda_{\text{emission}}$ of GAFluoroCoP in DMSO. The GAFluoroCoP-EDTA mixture therefore, didn't exhibit any quenching towards the normal fluorescence of GAFluoroCoP. However, no fluorescence quenching in SmGAFluoroCoP was observed in-presence of EDTA solution. Since EDTA is a stronger chelating ligand compared to GAFluoroCoP, Sm(III) preferentially binds with EDTA rather than GAFluoroCoP, resulting in the maintenance of the normal fluorescence behavior of GAFluoroCoP. This phenomenon can be described as a truth table of NOT and NAND gates with respect to EDTA and Sm(III), respectively (Table S8). Therefore, the complexation reaction between Sm(III) and GAFluoroCoP can be justified as the primary mechanism of fluorescence-quenching.

3.8. *Adsorptive recovery of high valued Sm (III)*

Adsorption is a surface phenomenon and is also guided by a number of factors, of which pH, adsorbent dose, temperature, and initial concentration of adsorbate are the major constraints. Therefore, to achieve the maximum adsorption capacity (q_{max}, mg g^{-1}), the above-mentioned parameters should be optimized. Herein, the effect of pH and adsorbent (i.e., GAFluoroCoP) dose was optimized by carrying out Sm(III)-adsorption experiments at 298 K and 50 ppm initial concentration of Sm(III). For pH optimization, adsorption experiments were conducted at variable pH from 2 to 8 by keeping the dose constant at 0.015 g (Fig. 7A), whereas for dose optimization, Sm(III)-adsorption experiments were carried out by using 0.01–0.02 g GAFluoroCoP at pH = 7 (Fig. 7B). Sm(III) starts precipitating out from as hydroxides in alkaline pH and therefore, we could not analyze the adsorption potential of GAFluoroCoP at pH beyond 8. From Fig. 7A, the q_{max} value was found to increase significantly with the increase in pH from 2 to 7, whereas some insignificant increase in q_{max} value could be observed at pH = 8. According to FT-IR and XPS, Sm(III) is mostly attached with GAFluoroCoP via ionic and/or coordinate bonding; anionic functionalities on GAFluoroCoP should be essential for successful adsorption. Since the pH_{PZC} of GAFluoroCoP was found to be 5.32, the surface of GAFluoroCoP started to become negative at pH > 5.32. Therefore, the q_{max} value increased with the increase in pH. However, due to the over-population of OH– ions, Sm(III) has the tendency to precipitate out as $Sm(OH)_3$ and thus no significant improvement in q_{max} value could be observed from pH = 7 to 8. Therefore, the pH could be optimized at pH = 7. For dose optimization, two opposing situations should be considered, viz. AC and %adsorption. AC decreases with the increase in dose, whereas %adsorption increases with the increase in dose. From Fig. 7B, the best balance between AC and %adsorption was found to be at 0.015 g. Therefore, the dose was optimized to be 0.015 g.

Isothermal adsorption experiments were carried out at four different

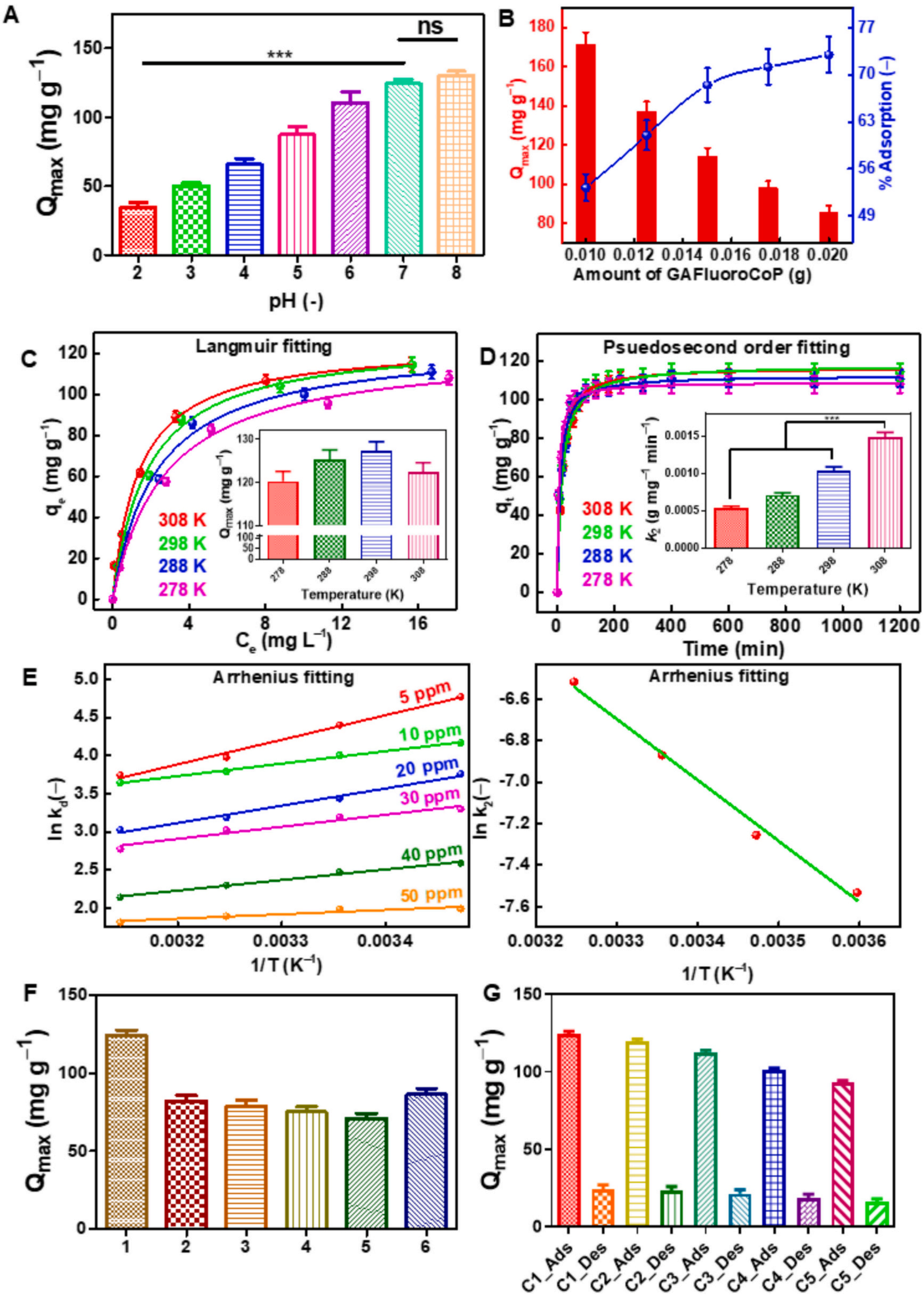

Fig. 7. Adsorption studies of Sm(III) by GAFluoroCoP: (A/B) pH/dose optimization experiments. (C-E) Isotherm, kinetics, and thermodynamics fitting data. (F) Selective adsorption of Sm(III) from binary mixtures. (G) Recyclabilitty studies of SmGAFluoroCoP through five adospriand-desorption cycles. Data are presented as mean ± SD ($n = 3$). Statistical significance was determined using one-way ANOVA followed by Tukey's post hoc test. $^{*}p < 0.05$ between indicated groups.

temperatures within 278–308 K to rationalize the ambient temperatures of most of the parts of the World. The equilibrium adsorption data were fitted to various isotherm models, such as Langmuir, Freundlich, Sips, Harkins-Jura etc., of which the Langmuir isotherm fitted the best in all temperatures (Fig. 7C). Therefore, the monolayer adsorption property could be understood. The q_{max} values were found to vary within 120.33 to 127.28 mg g^{-1}. However, the variation of q_{max} values with temperature was found to be insignificant. We then studied the isotherm kinetics experiments at four different temperatures within 278–308 K (Fig. 7D). The data best fitted with the pseudosecond order model rather than the pseudofirst order model, justifying the existence of chemisorption, as observed earlier from FT-IR and XPS analyses. From Fig. 7D, the k_2 values were found to increase significantly from 5.35 × 10–4 (g mg^{-1} min^{-1}) at 278 K to 14.80 × 10–4 (g mg^{-1} min^{-1}) at 308 K, suggesting the appearance of faster adsorption at the higher temperatures. Such a phenomenon could be further justified from the adsorption thermodynamics studies, where the ΔG^0 values appeared to be higher negative at the higher temperatures (Fig. 7E and Table S10). From

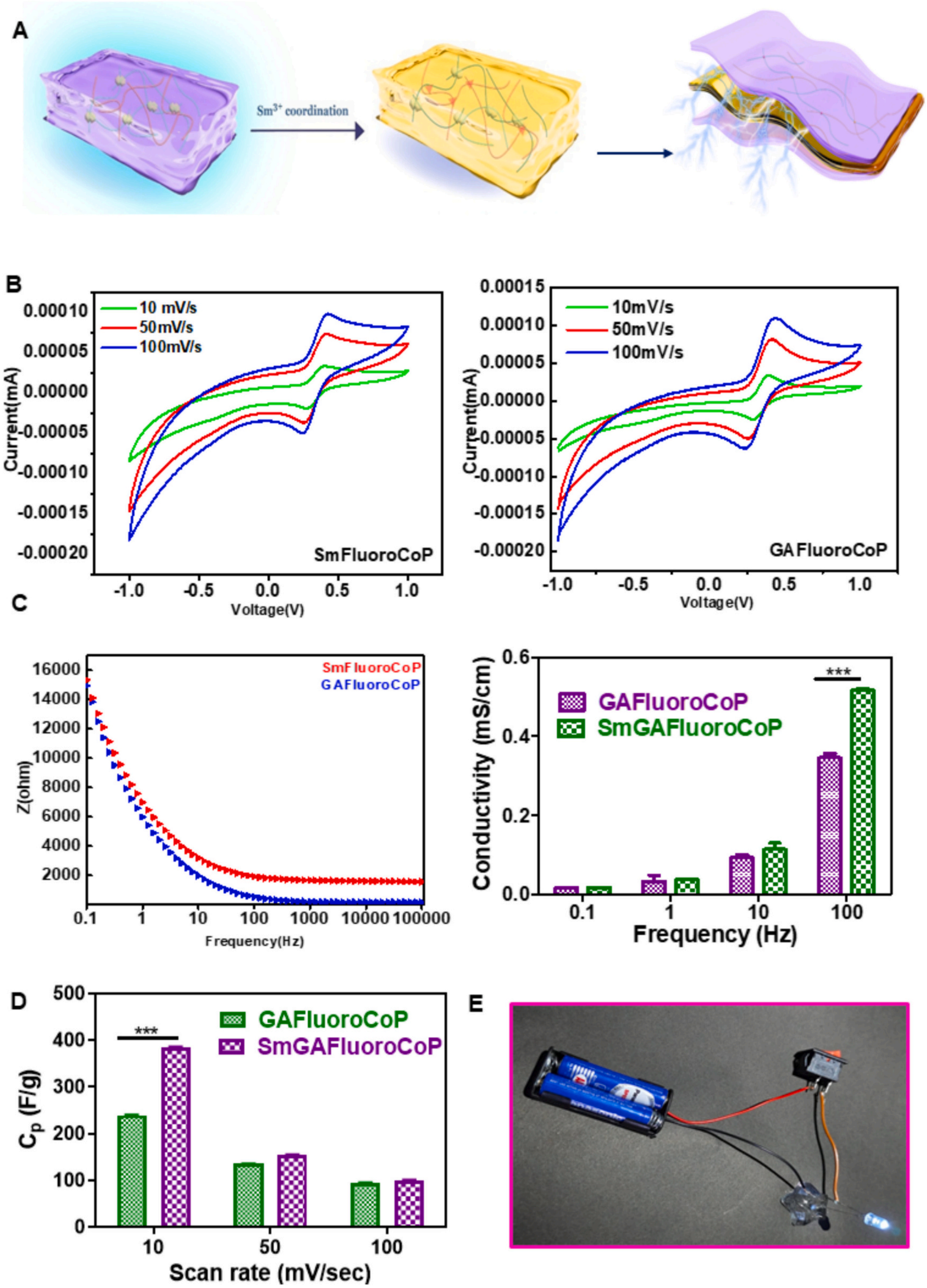

Fig. 8. Post-Adsorptive Application of SmGAFluoroCoP towards semiconducting properties: (A) Schematic illustration for Sm(III) coordination into GAFluoroCoP leading to modulation of its electrical behavior. (B) CV plots of GAFluoroCoP and SmGAFluoroCoP. (C) Bode plots and conductivity studies of GAFluoroCoP and SmGAFluoroCoP. (D) Comparison of specific capacitance values of GAFluoroCoP and SmGAFluoroCoP at various scan rates. (E) Bulb illumination image demonstrating the electrical conductivity of SmGAFluoroCoP.

Fig. 7E, the activation energy (E_a) value was found to be 25.78 kJ mol^{-1}, which confirmed the existence of chemisorption.

We then studied the selective adsorption of Sm(III) from its binary mixture with other REMs (Fig. 7F), a clear drop in the q_{max} values of Sm (III) could be observed at all the identical adsorption conditions. This observation could be explained from the competitive adsorption due to the common ion effect.

Next, we studied the desorption experiment of SmGAFluoroCoP at the opposite pH of the adsorption pH (Fig. 7G). More than 90% desorption efficiency inferred the practical utility of the recovered high-valued Sm(III) for further experiments. We also studied the repeated adsorption-desorption cycles at pH = 10 and 2, respectively, and at least five cycles could be studied clearly before GAFluoroCoP became fragile. The excellent adsorption capacity retention (> 90%) could be observed for GAFluoroCoP even at the fifth cycle of adsorption. Such observation inferred the excellent network stability of GAFluoroCoP, already observed from the physicochemical studies.

3.9. Post-adsorptive applications

3.9.1. Conductive property of GAFluoroCoP after metal ion loading

Most of the sensing and adsorption studies do not report any promising and safe disposal of metal ion-loaded adsorbent, which may further generate the probability of secondary pollution. In this context, we already mentioned the desorption of Sm(III) from SmGAFluoroCoP and the further use of the desorbed GAFluoroCoP. However, it is important to remember that Sm(III) is a very high-valued REE, and thus a few innovative post-adsorptive applications can be designed by using SmGAFluoroCoP. For instance, we studied the alteration in specific conductivity of GAFluoroCoP after Sm(III) adsorption (Fig. 8A). In the cyclic voltammetry (CV) experiment (Fig. 8B), the nearly symmetrical forward and reverse curves indicate good charging-discharging reversibility. Broadened redox peaks at lower scan rates suggest partial redox activity at the SmGAFluoroCoP electrodes, confirming a pseudocapacitive energy storage mechanism. At higher scan rates, the CV curves approach a rectangular shape, reflecting improved ion diffusion and capacitive behavior. At scan rates of 10, 50, and 100 mV/s, the specific capacitance of SmGAFluoroCoP was found to be 383.81, 153.80, and 99.83 mF cm^{-2}, respectively, which is significantly higher than the corresponding values for GAFluoroCoP, 239.18, 135.09, and 94.38 mF cm^{-2} (Fig. 8D). Also, from the Bode plot, the electrical conductivity of CoP / SmGAFluoroCoP were found to be 0.016/0.017, 0.032/0.038, 0.093/0.113, and 0.345/0.517 mS/cm at 0.1, 1, 10, and 100 Hz, respectively (Fig. 8C). The conductivity of SmGAFluoroCoP increased significantly upon complexation with Sm(III), enhancing its suitability for semiconducting applications. This improvement can be attributed to the availability of free electrons introduced by the metal ions within the GAFluoroCoP matrix. In the literature, the acrylic-based hydrogels are reported to possess diverse conductivity values [87,88]. We further demonstrated the electrical conductivity of the hydrogel through LED illumination in a closed circuit powered by AA cells, confirming its ability to facilitate electron transport (Fig. 8E). Therefore, SmGAFluoroCoP is also capable of transmitting bioelectrical signals in response to the endogenous electric fields in tumor therapy. Semiconducting behavior of GAFluoroCoP after Sm(III) doping was evaluated by band gap (E_g)calculation (Table S10). SmGAFluoroCoP exhibited a band gap of 1.44 eV, which is the optimum range for semiconducting materials. Such improvements in semiconducting behavior are primarily attributed to electronic structure alterations that facilitate increased charge carrier mobility and density [89].This makes this doped SmGAFluoroCoP well suited for versatile electronic applications.

We then evaluated the bending durability of the conductive SmGAFluoroCoP by measuring the normalized change in resistance ($\Delta R/R_o$) during repeated bending [here R_o represents the initial resistance before applying mechanical stress]. For better understanding of the stability of SmGAFluoroCoP over 100 cycles, the device was subjected to 500 consecutive bending-release cycles while the resistance was recorded continuously, and the time points were reindexed as cycle numbers (Fig. S21). Over this entire range, $\Delta R/R_o$ fluctuated around an average value of ~0.10 with small noise-like variations within −0.10 to 0.25 excluding any systematic drift or cumulative increase. Specifically, at the first 100 cycles, the $\Delta R/R_o$ pattern remained almost unaltered, inferring excellent stability of the electrical pathway of SmGAFluoroCoP over bending. In fact, bending does not induce any significant fatigue or permanent damage in this regime. Such observation demonstrates that SmGAFluoroCoP can maintain stable conductivity during extreme flexing and meet the durability criteria commonly adopted in high-performance flexible and wearable electronic systems.

3.9.2. Anti-tumorigenesis properties of SmGAFluoroCoP via over oxidative stress

We then studied the time-dependent ROS-generation potential of GAFluoroCoP and SmGAFluoroCoP to determine any anti-tumorigenesis effect developed in SmGAFluoroCoP. According to the XPS and FT-IR analyses, Sm(III) is attached with GAFluoroCoP through ionic and/or coordinate bonding. Therefore, the electronic transition between Sm(III) and GAFluoroCoP should be active, and this has inspired us to study the ROS generation studies (Fig. 9A). According to the H_2O_2 and TMB assay, the control group possessed the lowest generation of ROS of 2.98% (Fig. 9B). Some significant improvement in H_2O_2 generation could be observed for CoP, suggesting the negligible contribution of ROS generation. However, SmGAFluoroCoP exhibited stronger H_2O_2 generation (51.96%) than those of Control and GAFluoroCoP. From the MTT assay, the increase in cytotoxicity could be visualized for SmGAFluoroCoP compared to GAFluoroCoP (Fig. S22).

To confirm the cellular uptake of Sm(III) from SmGAFluoroCoP, resulting in the formation of oxidative stress in cells, 2,7-dichlorodihydrofluorescein diacetate (DCFH-DA) probe was utilized to observe the presence of H_2O_2 within cells (Fig. 9C). Mechanistically, DCFH-DA is consumed by the cells, followed by its conversion into DCFH via cleaving off the acetyl groups by the cellular esterase. Thereafter, oxidized DCFH can emit green fluorescence in the presence of H_2O_2. Therefore, the intensity of green fluorescence can quantify the concentration of H_2O_2 (representative ROS) [90,91]. Herein, the stronger green fluorescence intensity of SmGAFluoroCoP compared to GAFluoroCoP inferred the higher ROS generation capacity of SmGAFluoroCoP. Moreover, the strong H_2O_2 generation phenomenon of Sm(III) doped hydrogel remains unreported in the literature. The radical generation ability of SmGAFluoroCoP and GAFluoroCoP was further confirmed by electron paramagnetic resonance (EPR) analysis (Fig. 9D). The strongest characteristic 1:2:2:1 signal ratio of $^{\bullet}OH$ could be observed from the EPR signal of SmGAFluoroCoP, which ensured the formation of $^{\bullet}OH$ from H_2O_2. Therefore, the generation of oxidative stress from SmGAFluoroCoP is evident. Also, to observe the effect of such generated oxidative stress on tumor cells, an intracellular live/dead assay was performed on MDCK cells (tumor cells). The control group exhibited strong green fluorescence, indicating a high number of viable cells. In contrast, the sample group showed predominant red fluorescence, signifying a high rate of apoptosis. Notably, samples containing Sm-incorporated GAFluoroCoP displayed significantly elevated apoptotic activity, highlighting their promising potential for tumor Therapy. Also, we quantitatively evaluated the fluorescence intensities of all the groups (Fig. 9E). These data inferred the excellent ROS generation property of SmGAFluoroCoP > Control >GAFluoroCoP with respect to MDCK cells.

4. Conclusions

This research demonstrated the successful fabrication of a multifunctional fluorescent interpenetrating network hydrogel, GAFluoroCoP, that enables selective sensing and efficient recovery of Sm(III), along with promising post-adsorptive applications in semiconductor applications, tumor therapy, and other clinical applications. The

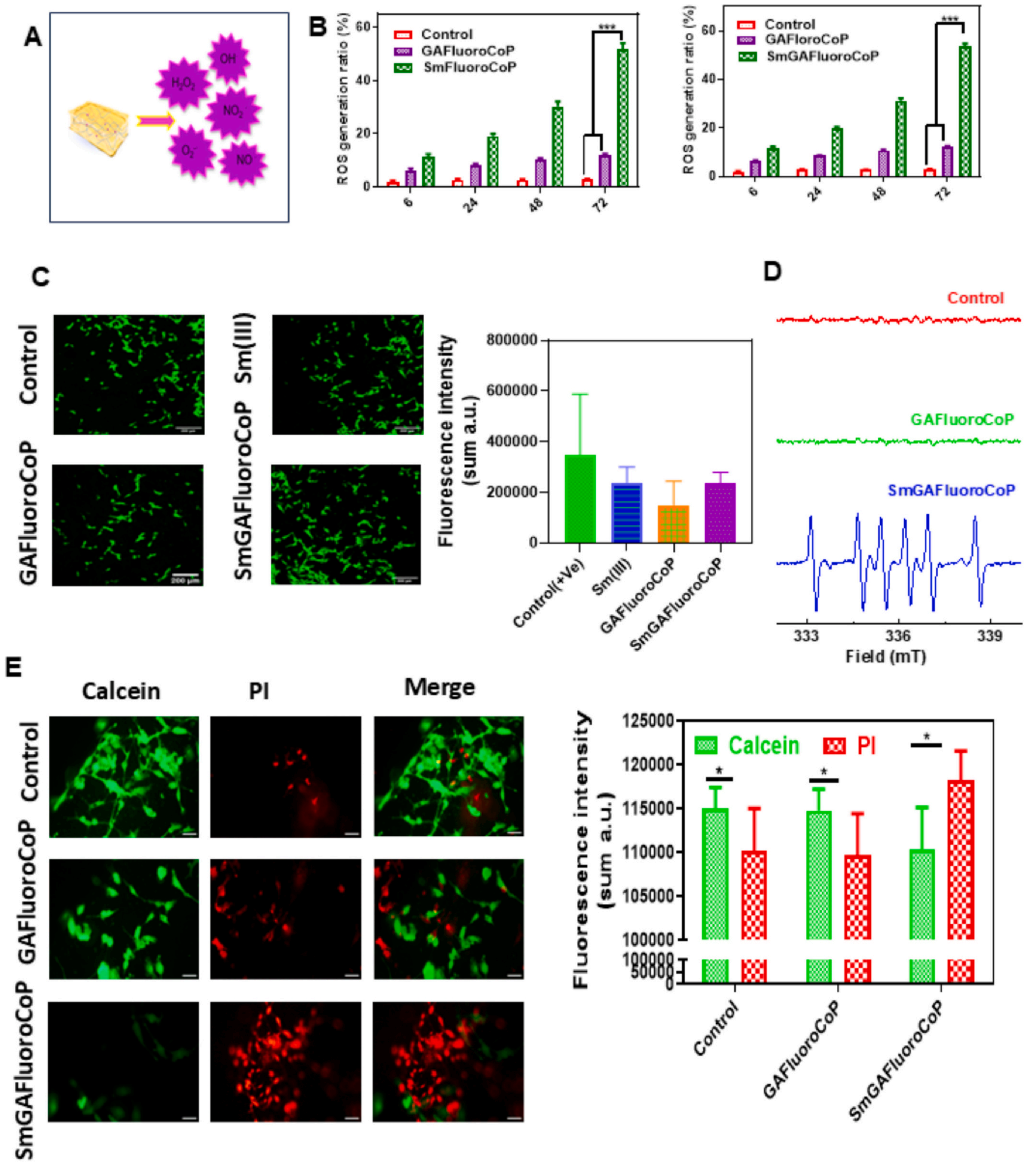

Fig. 9. Post-Adsorptive application of SmGAFluoroCoP in ROS-mediated apoptosis: (A) Schematic illustration of the ROS-generation mechanism. (B) In vitro H_2O_2 and TMB assays. (C) DCFH-DA assay for ROS generation along with fluorescence intensity quantification in Sm(III), GAFluoroCoP and SmGAFluoroCoP with respect to the control. (D) EPR spectra of GAFluoroCoP and SmGAFluoroCoP with respect to the control. (E) Fluorescence-based live/dead assay on MDCK cells to prove apoptosis. Each point represents mean ± SD ($n = 3$). Statistical significance was determined using one-way ANOVA followed by Tukey's post hoc test. $^{*}p < 0.05$ between indicated groups.

hydrogel exhibits excellent environmental responsiveness, evidenced by rapid super-adsorption of Sm(III) from REE mixtures, and remarkable fluorescence quenching with a detection limit as low as 37.5 picoM. The robust gelation achieved across a broad temperature range (273–323 K), coupled with consistent ESR values, highlights the ambient adaptability of the synthesis protocol. GAFluoroCoP showcases superior mechanical toughness, self-healing ability, and recyclability across multiple cycles, enabled by its dynamic polymeric network. Notably, its strong adhesiveness to various substrates under moist conditions supports its potential use in industrial applications.

The hydrogel's high swelling capacity, rapid polymerization (~50 s), and chemisorption-driven uptake behavior ($q_{max} = 127.28$ mg g^{-1}.) further validate its suitability for real-world remediation scenarios. Beyond adsorption, the successful conversion of GAFluoroCoP into a semiconducting material ($E_{gap} = 1.44$ eV) and its ROS-generating capability underscore its potential in electronics and anti-tumor therapeutics.

CRediT authorship contribution statement

Somya Sadaf: Writing – original draft, Visualization, Validation, Software, Methodology, Investigation, Funding acquisition, Formal analysis, Data curation, Conceptualization. **Mrinmoy Karmakar:** Writing – review & editing, Validation, Methodology, Formal analysis, Data curation. **Yati Sharma:** Software. **Anirban Mandal:** Software. **Chinmay Ghoroi:** Writing – review & editing, Supervision, Resources, Funding acquisition, Conceptualization.

Declaration of competing interest

The authors declare that they have no financial or personal relationships that could be perceived as potential conflicts of interest affecting the research reported in this article.

Acknowledgements

This work was supported by DSIR-IITGN Common Research & Technology Development Hub (Grant No. DSIR/CRTDH/NM/IIT-Gn/2016) and the Central Instrumentation Facility at IIT Gandhinagar for access to instrumentation. The authors would like to express their gratitude to the B. S. Gelot Chair for the valuable support provided for this work. S.S. is thankful for the financial support received through the Prime Minister's Research Fellowship (MIS/IITGN/PMRF/CL/CG/2023-24/048). M.K. is grateful to IIT Gandhinagar for providing postdoctoral fellowship. The authors are grateful to Professor Sriram Kanvah Gundimeda, Department of Chemistry, Indian Institute of Technology Gandhinagar, for allowing to use the TCSPC instrument. During the preparation of this work, the author(s) used Generative AI to assist with language clarity and refinement, ensuring coherence and consistency in the content. The AI tool was not used for data analysis, interpretation, or any intellectual contributions. The authors have carefully reviewed and revised the content generated with this Generative AI tool and take full responsibility for the accuracy, integrity, and final presentation of the article.

Appendix A. Supplementary data

Supplementary data to this article can be found online at https://doi.org/10.1016/j.cej.2026.172857.

Data availability

Data will be made available on request.

References

[1] L. Depraiter, S. Goutte, The role and challenges of rare earths in the energy transition, Res. Policy 86 (2023) 104137, https://doi.org/10.1016/J.RESOURPOL.2023.104137.

[2] V. Balaram, Rare earth elements: a review of applications, occurrence, exploration, analysis, recycling, and environmental impact, Geosci. Front. 10 (2019) 1285–1303, https://doi.org/10.1016/J.GSF.2018.12.005.

[3] L. Depraiter, S. Goutte, T. Porcher, Geopolitical risk and the global supply of rare earth permanent magnets: insights from China's export trends, Energy Econ. 146 (2025) 108496, https://doi.org/10.1016/J.ENECO.2025.108496.

[4] Z. Ge, Y. Geng, W. Wei, C. Zhong, Assessing samarium resource efficiency in China: a dynamic material flow analysis, Res. Policy 76 (2022) 102638, https://doi.org/10.1016/J.RESOURPOL.2022.102638.

[5] Y. Ghorbani, I.M.S.K. Ilankoon, N. Dushyantha, G.T. Nwaila, Rare earth permanent magnets for the green energy transition: bottlenecks, current developments and cleaner production solutions, Resour. Conserv. Recycl. 212 (2025) 107966, https://doi.org/10.1016/J.RESCONREC.2024.107966.

[6] O. Gutfleisch, M.A. Willard, E. Brück, C.H. Chen, S.G. Sankar, J.P. Liu, Magnetic materials and devices for the 21st century: stronger, lighter, and more energy efficient, Adv. Mater. 23 (2011) 821–842, https://doi.org/10.1002/adma.201002180.

[7] O. Moreira, Analysis of 149Sm time evolution and the reactivity contribution in nuclear reactors, Ann. Nucl. Energy 83 (2015) 87–93, https://doi.org/10.1016/J.ANUCENE.2015.04.009.

[8] G. Okada, J. Ueda, S. Tanabe, G. Belev, T. Wysokinski, D. Chapman, D. Tonchev, S. Kasap, Samarium-doped oxyfluoride glass-ceramic as a new fast erasable dosimetric detector material for microbeam radiation cancer therapy applications at the Canadian synchrotron, J. Am. Ceram. Soc. 97 (2014) 2147–2153, https://doi.org/10.1111/jace.12938.

[9] H.A. Saudi, H.O. Tekin, H.M.H. Zakaly, S.A.M. Issa, G. Susoy, M. Zhukovsky, The impact of samarium (III) oxide on structural, optical and radiation shielding properties of thallium-borate glasses: experimental and numerical investigation, Opt Mater (Amst) 114 (2021) 110948, https://doi.org/10.1016/J.OPTMAT.2021.110948.

[10] T. Baskaran, S.B. Arya, Role of thermally grown oxide and oxidation resistance of samarium strontium aluminate based air plasma sprayed ceramic thermal barrier coatings, Surf. Coat. Technol. 326 (2017) 299–309, https://doi.org/10.1016/J.SURFCOAT.2017.07.049.

[11] M. Sattar, S. Anjum, M.Y. Raja, Z. Mustafa, A. Mansoor, R. Khurram, T. Ilayas, Samarium substituted M-type Sr hexaferrites: the structural, magnetic and electrochemical properties for supercapacitor applications, Ceram. Int. 50 (2024) 16747–16764, https://doi.org/10.1016/J.CERAMINT.2024.01.224.

[12] Z. Jing, Q. Du, X. Zhang, Y. Zhang, Nanomedicines and nanomaterials for cancer therapy: Progress, challenge and perspectives, Chem. Eng. J. 446 (2022) 137147, https://doi.org/10.1016/J.CEJ.2022.137147.

[13] H.Y. Tan, Y.H. Wong, A. Kasbollah, M.N.M. Shah, B.J.J. Abdullah, A.C. Perkins, C. H. Yeong, Biodistribution and long-term toxicity of neutron-activated Samarium-153 oxide-loaded polystyrene microspheres in healthy rats, Nucl. Med. Biol. 146–147 (2025) 109026, https://doi.org/10.1016/J.NUCMEDBIO.2025.109026.

[14] REPORT ON CRITICAL RAW MATERIALS FOR THE EU, 2014.

[15] U. Department of Energy, Notice of Final Determination on 2023 DOE Critical Materials List, n.d.

[16] FOR INDIA CRITICAL MINERALS Ministry of Mines June 2023 Report of the Committee on Identification of Critical Minerals, n.d.

[17] X. Li, Z. Li, M. Orefice, K. Binnemans, Metal recovery from spent samarium-cobalt magnets using a Trichloride ionic liquid, ACS Sustain. Chem. Eng. 7 (2019) 2578–2584, https://doi.org/10.1021/acssuschemeng.8b05604.

[18] K. Liu, Q. Tan, J. Yu, M. Wang, A global perspective on e-waste recycling, Circular Economy 2 (2023) 100028, https://doi.org/10.1016/J.CEC.2023.100028.

[19] V. Kaim, J. Rintala, C. He, Selective recovery of rare earth elements from e-waste via ionic liquid extraction: a review, Sep. Purif. Technol. 306 (2023) 122699, https://doi.org/10.1016/J.SEPPUR.2022.122699.

[20] C. Blaise, F. Gagné, M. Harwood, B. Quinn, H. Hanana, Ecotoxicity responses of the freshwater cnidarian Hydra attenuata to 11 rare earth elements, Ecotoxicol. Environ. Saf. 163 (2018) 486–491, https://doi.org/10.1016/J.ECOENV.2018.07.033.

[21] Y. Liu, R. Pu, B. Zou, X. Zhang, X. Wang, H. Yin, J. Jin, Y. Xie, Y. Sun, X. Jia, Y. Bi, Samarium oxide exposure induces toxicity and cardiotoxicity in zebrafish embryos through apoptosis pathway, J. Appl. Toxicol. (2025), https://doi.org/10.1002/jat.4774.

[22] K. Hu, Y. Liu, X. Zhou, S. Hussain, K. Li, Q. Chen, C. Zhang, W. Song, X. Li, Y. Wan, Highly selective recovery of rare earth elements from mine wastewater by modifying kaolin with phosphoric acid, Sep. Purif. Technol. 309 (2023) 123117, https://doi.org/10.1016/J.SEPPUR.2023.123117.

[23] O. Artiushenko, R.F. da Silva, V. Zaitsev, Recent advances in functional materials for rare earth recovery: a review, Sustain. Mater. Technol. 37 (2023) e00681, https://doi.org/10.1016/J.SUSMAT.2023.E00681.

[24] B. Cai, L. Gandon, C. Baratange, O. Eyeleye, R. Moncrieffe, G. Montiel, A. Kamari, S. Bertrand, M.-J. Durand, L. Poirier, P. Deleris, A. Zalouk-Vergnoux, Assessment of the effects of cadmium, samarium and gadolinium on the blue mussel (Mytilus edulis): a biochemical, transcriptomic and metabolomic approach, Aquat. Toxicol. 279 (2025) 107217, https://doi.org/10.1016/J.AQUATOX.2024.107217.

[25] H. Hanana, C. Kleinert, F. Gagné, Toxicity of Representative Mixture of Five Rare Earth Elements in Juvenile Rainbow Trout (*Oncorhynchus mykiss*) Juveniles, (n.d.). doi:https://doi.org/10.1007/s11356-020-12218-5/Published.

[26] D.Y. Zhang, X.Y. Shen, Q. Ruan, X.L. Xu, S.P. Yang, Y. Lu, H.Y. Xu, F.L. Hao, Effects of subchronic samarium exposure on the histopathological structure and apoptosis regulation in mouse testis, Environ. Toxicol. Pharmacol. 37 (2014) 505–512, https://doi.org/10.1016/J.ETAP.2014.01.007.

[27] K.T. Rim, K.H. Koo, J.S. Park, Toxicological evaluations of rare earths and their health impacts to workers: a literature review, Saf. Health Work 4 (2013) 12–26, https://doi.org/10.5491/SHAW.2013.4.1.12.

[28] S.J. Buchanan, L.S. Dale, Inductively coupled plasma-atomic emission spectrometric determination of rare earth elements in geological materials, Spectrochim Acta part B at, Spectrosc 41 (1986) 237–242, https://doi.org/10.1016/0584-8547(86)80163-X.

[29] M.C. Bruzzoniti, E. Mentasti, C. Sarzanini, M. Braglia, G. Cocito, J. Kraus, Determination of rare earth elements by ion chromatography, Separation procedure optimization, Anal Chim Acta 322 (1996) 49–54, https://doi.org/10.1016/0003-2670(95)00596-X.

[30] N. Shokoufi, J. Yoosefian, Selective determination of Sm (III) in lanthanide mixtures by thermal lens microscopy, J. Ind. Eng. Chem. 35 (2016) 153–157, https://doi.org/10.1016/J.JIEC.2015.12.027.

[31] C. Andrew, M. Dhivya, M. Jayakumar, Electrochemical and spectroscopic investigation of samarium in a neutral ligand based-ionic liquid, J. Electroanal. Chem. 895 (2021) 115398, https://doi.org/10.1016/J.JELECHEM.2021.115398.

[32] R. Pramanik, A review on fluorescent molecular probes for Hg2+ ion detection: mechanisms, strategies, and future directions, ChemistrySelect 10 (2025), https://doi.org/10.1002/slct.202404525.

[33] J. Li, G. Chen, Y. Zeng, Simultaneous determination of Dy, Eu, Sm and Tb by laser induced-time resolved derivative fluorescence, Fresenius J. Anal. Chem. 336 (1990) 139–142, https://doi.org/10.1007/BF00322554.

[34] Z. Hassankhani-Majd, M. Anbia, Recovery of valuable materials from phosphorus slag using nitric acid leaching followed by precipitation method, Resour. Conserv. Recycl. 169 (2021) 105547, https://doi.org/10.1016/J.RESCONREC.2021.105547.

[35] K. Hu, H. Gao, Y. Nie, H. Dong, J. Yan, X. Zhang, F. Li, Efficient selective separation of yttrium from holmium and erbium using carboxyl functionalized ionic liquids, Sep. Purif. Technol. 269 (2021) 118774, https://doi.org/10.1016/J.SEPPUR.2021.118774.

[36] K. Hu, L. Xing, Y. Nie, X. Li, H. Dong, H. Gao, Removal of aluminum to obtain high purity gadolinium with pyridinium-based ionic liquids, Hydrometallurgy 213 (2022) 105930, https://doi.org/10.1016/J.HYDROMET.2022.105930.

[37] D.M. Park, A. Brewer, D.W. Reed, L.N. Lammers, Y. Jiao, Recovery of rare earth elements from low-grade feedstock leachates using engineered Bacteria, Environ. Sci. Technol. 51 (2017) 13471–13480, https://doi.org/10.1021/acs.est.7b02414.

[38] T. Kegl, A. Košak, A. Lobnik, Z. Novak, A.K. Kralj, I. Ban, Adsorption of rare earth metals from wastewater by nanomaterials: a review, J. Hazard. Mater. 386 (2020) 121632, https://doi.org/10.1016/J.JHAZMAT.2019.121632.

[39] X. Yang, D.K. Debeli, G. Shan, P. Pan, Selective adsorption and high recovery of La3+ using graphene oxide/poly (N-isopropyl acrylamide-maleic acid) cryogel, Chem. Eng. J. 379 (2020) 122335, https://doi.org/10.1016/J.CEJ.2019.122335.

[40] J. Cheng, X. Hua, G. Zhang, M. Yu, Z. Wang, Y. Zhang, W. Liu, Y. Chen, H. Wang, Y. Luo, X. Hou, X. Xie, Synthesis of high-crystallinity zeolite a from rare earth tailings: investigating adsorption performance on typical pollutants in rare earth mines, J. Hazard. Mater. 468 (2024) 133730, https://doi.org/10.1016/J.JHAZMAT.2024.133730.

[41] M.S. Hossain, M.A. Shenashen, M.E. Awual, A.I. Rehan, A.I. Rasee, R.M. Waliullah, K.T. Kubra, M.S. Salman, M.C. Sheikh, M.N. Hasan, M.M. Hasan, A. Islam, M. A. Khaleque, H.M. Marwani, K.A. Alzahrani, A.M. Asiri, M.M. Rahman, M. R. Awual, Benign separation, adsorption, and recovery of rare-earth Yb(III) ions with specific ligand-based composite adsorbent, Process. Saf. Environ. Prot. 185 (2024) 367–374, https://doi.org/10.1016/J.PSEP.2024.03.026.

[42] W. Song, B. Gao, X. Xu, L. Xing, S. Han, P. Duan, W. Song, R. Jia, Adsorption–desorption behavior of magnetic amine/Fe3O4 functionalized biopolymer resin towards anionic dyes from wastewater, Bioresour. Technol. 210 (2016) 123–130, https://doi.org/10.1016/J.BIORTECH.2016.01.078.

[43] S. Satyam, S. Patra, Innovations and challenges in adsorption-based wastewater remediation: a comprehensive review, Heliyon 10 (2024), https://doi.org/10.1016/j.heliyon.2024.e29573.

[44] K. Momina, Ahmad, feasibility of the adsorption as a process for its large scale adoption across industries for the treatment of wastewater: research gaps and economic assessment, J clean, Prod 388 (2023) 136014, https://doi.org/10.1016/J.JCLEPRO.2023.136014.

[45] A.K. Tolkou, E.K. Tsoutsa, G.Z. Kyzas, I.A. Katsoyiannis, Sustainable use of low-cost adsorbents prepared from waste fruit peels for the removal of selected reactive and basic dyes found in wastewaters, Environ. Sci. Pollut. Res. 31 (2024) 14662–14689, https://doi.org/10.1007/s11356-024-31868-3.

[46] K. Mohanrasu, A.C. Manivannan, H.J.R. Rengarajan, R. Kandaiah, A. Ravindran, L. Panneerselvan, T. Palanisami, C.I. Sathish, Eco-friendly biopolymers and composites: a sustainable development of adsorbents for the removal of pollutants from wastewater, Npj Materials Sustainability 3 (2025) 13, https://doi.org/10.1038/s44296-025-00057-9.

[47] R. Jayasree, P.S. Kumar, A. Saravanan, R.V. Hemavathy, P.R. Yaashikaa, P. Arthi, J. Shreshta, S. Jeevanantham, S. Karishma, M.V. Arasu, N.A. Al-Dhabi, K.C. Choi, Sequestration of toxic Pb(II) ions using ultrasonic modified agro waste: adsorption mechanism and modelling study, Chemosphere 285 (2021) 131502, https://doi.org/10.1016/J.CHEMOSPHERE.2021.131502.

[48] S. Liu, Y. Kang, Synergistic oxidation induced by underwater bubbling plasma and diatomite-CoFe2O4 activated peroxymonosulfate for the degradation of ciprofloxacin hydrochloride, Environ. Pollut. 348 (2024) 123891, https://doi.org/10.1016/J.ENVPOL.2024.123891.

[49] N. Sheraz, A. Shah, A. Haleem, F.J. Iftikhar, Comprehensive assessment of carbon-, biomaterial- and inorganic-based adsorbents for the removal of the most hazardous heavy metal ions from wastewater, RSC Adv. 14 (2024) 11284–11310, https://doi.org/10.1039/d4ra00976b.

[50] L. Hadjittofi, S. Charalambous, I. Pashalidis, Removal of trivalent samarium from aqueous solutions by activated biochar derived from cactus fibres, J. Rare Earths 34 (2016) 99–104, https://doi.org/10.1016/S1002-0721(14)60584-6.

[51] A.I. Rasee, E. Awual, A.I. Rehan, M.S. Hossain, R.M. Waliullah, K.T. Kubra, M. C. Sheikh, M.S. Salman, M.N. Hasan, M.M. Hasan, H.M. Marwani, A. Islam, M. A. Khaleque, M.R. Awual, Efficient separation, adsorption, and recovery of samarium(III) ions using novel ligand-based composite adsorbent, Surf. Interfaces 41 (2023) 103276, https://doi.org/10.1016/J.SURFIN.2023.103276.

[52] S. Jovanovic, D. Kepic, Chitosan Polymers: Their Blends, <scp>IPNs</scp>, Gels, and Composites Membranes for Water Purification, in: Biopolymers for Water Purification, Wiley, 2025, pp. 301–340, https://doi.org/10.1002/9783527835904.ch10.

[53] Z. Ahamad, A.S. Bhat, A. Nasar, High-performance magnetic graphene oxide/alginate hydrogel for efficient malachite green removal, J. Water Process Eng. 70 (2025) 107024, https://doi.org/10.1016/J.JWPE.2025.107024.

[54] P.S. Gahlaut, D. Gautam, K. Yadav, B. Jana, Supramolecular gels for the sensing and extraction of heavy metal ions from wastewater, J. Mol. Struct. 1272 (2023) 134152, https://doi.org/10.1016/J.MOLSTRUC.2022.134152.

[55] T. Rani Sethy, T. Biswal, P. Kumar Sahoo, An indigenous tool for the adsorption of rare earth metal ions from the spent magnet e-waste: an eco-friendly chitosan biopolymer nanocomposite hydrogel, Sep. Purif. Technol. 309 (2023) 122935, https://doi.org/10.1016/J.SEPPUR.2022.122935.

[56] Y. Zhang, J. Luo, H. Zhang, T. Li, H. Xu, Y. Sun, X. Gu, X. Hu, B. Gao, Synthesis and adsorption performance of three-dimensional gels assembled by carbon nanomaterials for heavy metal removal from water: a review, Sci. Total Environ. 852 (2022) 158201, https://doi.org/10.1016/J.SCITOTENV.2022.158201.

[57] M. Karmakar, S. Sadaf, C. Ghoroi, pH-responsive biocompatible fluorescent hydrogel for selective sensing and adsorptive recovery of dysprosium, ACS Omega 9 (2024) 29620–29632, https://doi.org/10.1021/acsomega.4c02772.

[58] H. Chen, X.-Q. Zhan, Z.-L. Hong, W. Ni, C.-C. Zhu, Y.-P. Leng, C.-C. Chen, R.-T. Guo, N. Ma, F.-C. Tsai, Hydrogel-based sensor for the detection of Iron ions and excessive alerting, Langmuir 40 (2024) 26714–26722, https://doi.org/10.1021/acs.langmuir.4c03872.

[59] P. Yadav, S.G. Warkar, A. Kumar, Biopolymer-CMTG and m-BPDM based hydrogel composite for promising sensing of zinc, Cadmium, and Mercury in Aqueous Medium, J Inorg Organomet Polym Mater 35 (2025) 846–862, https://doi.org/10.1007/s10904-024-03224-y.

[60] A. Rahmatpour, A.H. Alizadeh, Biofilm hydrogel derived from physical crosslinking (self-assembly) of xanthan gum and chitosan for removing Cd2+, Ni2+, and Cu2+ from aqueous solution, Int. J. Biol. Macromol. 266 (2024) 131394, https://doi.org/10.1016/J.IJBIOMAC.2024.131394.

[61] M. Chen, A. Long, W. Zhang, Z. Wang, X. Xiao, Y. Gao, L. Zhou, Y. Li, J. Wang, S. Sun, M. Tang, Y. Peng, H. Wang, Recent advances in alginate-based hydrogels for the adsorption–desorption of heavy metal ions from water: a review, Sep. Purif. Technol. 353 (2025) 128265, https://doi.org/10.1016/J.SEPPUR.2024.128265.

[62] C. Zhang, W. Chen, G. Owens, Z. Chen, Recovery of rare earth elements from mine wastewater using alginate microspheres encapsulated with zeolitic imidazolate framework-8, J. Hazard. Mater. 471 (2024) 134435, https://doi.org/10.1016/J.JHAZMAT.2024.134435.

[63] A.R. Salem, E.S.A. Haggag, M.M. Mohamed, G.A. Mahmoud, Efficient adsorption of lanthanum (III) and yttrium (III) ions using polyvinyl alcohol/polyvinylpyrrolidone/polyacrylamide terpolymer hydrogel, Surf. Interfaces 59 (2025) 105801, https://doi.org/10.1016/J.SURFIN.2025.105801.

[64] J. Wang, X. Lan, W. Shi, Z. Chen, Alginate-based hydrogel beads for ultrasensitive detection and effective adsorption of terbium and europium in water, Carbohydr. Polym. 353 (2025) 123258, https://doi.org/10.1016/J.CARBPOL.2025.123258.

[65] X. Fan, Z. Wang, Z. Lv, S. Han, G. Fan, W. Wang, Y. Cao, P. Li, D. Teng, Chitosan/kaolinite composite hydrogel with high mechanical strength for efficient and selective removal of copper ions: toward sustainable resource valorization, Carbohydr. Polym. 366 (2025) 123831, https://doi.org/10.1016/J.CARBPOL.2025.123831.

[66] M. Karmakar, S. Kim, H.J. Kim, J.W. Huh, D.I. Jeong, E. Park, S. Kim, E.-H. Hong, J. Hyeong, D.-J. Kim, H.K. Choi, J. Lee, H.-J. Ko, K.-B. Lee, D.-D. Kim, H.J. Cho, Spatiotemporally adjustable hybrid hydrogels interconnected by 2D MXene for combinatorial therapy of infected diabetic wounds, Chem. Eng. J. (2025) 167327, https://doi.org/10.1016/j.cej.2024.149315.

[67] S. Kim, J.H. Ahn, D.I. Jeong, M. Yang, J.H. Jeong, Y.E. Choi, H.J. Kim, Y. Han, M. Karmakar, H.J. Ko, H.J. Cho, Alum-tuned hyaluronic acid-based hydrogel with immune checkpoint inhibition for immunophoto therapy of cancer, J. Control. Release 362 (2023) 1–18, https://doi.org/10.1016/J.JCONREL.2023.08.027.

[68] Q. Lv, M. Wu, Y. Shen, Enhanced swelling ratio and water retention capacity for novel super-absorbent hydrogel, Colloids Surf. A Physicochem. Eng. Asp. 583 (2019) 123972, https://doi.org/10.1016/j.colsurfa.2019.123972.

[69] M. Karmakar, H. Mondal, M. Mahapatra, P.K. Chattopadhyay, S. Chatterjee, N. R. Singha, Pectin-grafted terpolymer superadsorbent via N–H activated strategic protrusion of monomer for removals of Cd(II), Hg(II), and Pb(II), Carbohydr. Polym. 206 (2019) 778–791, https://doi.org/10.1016/j.carbpol.2018.11.032.

[70] M. Mozaffari Majd, V. Kordzadeh-Kermani, V. Ghalandari, A. Askari, M. Sillanpää, Adsorption isotherm models: a comprehensive and systematic review

(2010−2020), Sci. Total Environ. 812 (2022) 151334, https://doi.org/10.1016/j.scitotenv.2021.151334.

[71] A.Ch. Lazanas, M.I. Prodromidis, Electrochemical Impedance Spectroscopy—A Tutorial, ACS Measurement Science Au 3 (2023) 162–193, https://doi.org/10.1021/acsmeasuresciau.2c00070.

[72] H. Jiang, L. Yang, C. Li, C. Yan, P.S. Lee, J. Ma, High–rate electrochemical capacitors from highly graphitic carbon–tipped manganese oxide/mesoporous carbon/manganese oxide hybrid nanowires, Energy Environ. Sci. 4 (2011) 1813, https://doi.org/10.1039/c1ee01032h.

[73] C. Hwang, Y.E. Choi, S.Y. Lee, M. Karmakar, Q. Hao, J. Lee, H. Cho, Self-Cascade catalytic reaction–assisted apoptosis/calcicoptosis/ferroptosis induction with microsphere-aggregated hydrogels in triple-negative breast cancer therapy, Adv. Funct. Mater. (2025), https://doi.org/10.1002/adfm.202420430.

[74] H. Mondal, M. Karmakar, B. Datta, Ligand-selective turn-off sensing, harvesting and post-adsorptive use of Dy(III) and Yb(III) by intrinsically fluorescent flower-shaped gum Acacia-grafted hydrogels, Sci. Rep. 14 (2024), https://doi.org/10.1038/s41598-024-65932-2.

[75] M. Bashir, S. Haripriya, Assessment of physical and structural characteristics of almond gum, Int. J. Biol. Macromol. 93 (2016) 476–482, https://doi.org/10.1016/j.ijbiomac.2016.09.009.

[76] T. Jayaramudu, R.D. Pyarasani, A. Akbari-Fakhrabadi, D. Abril-Milan, J. Amalraj, Synthesis of gum Acacia capped polyaniline-based nanocomposite hydrogel for the removal of methylene blue dye, J. Polym. Environ. 29 (2021) 2447–2462, https://doi.org/10.1007/s10924-021-02066-w.

[77] A.M.A. Hasan, M. Keshawy, M.E.S. Abdel-Raouf, Atomic force microscopy investigation of smart superabsorbent hydrogels based on carboxymethyl guar gum: surface topography and swelling properties, Mater. Chem. Phys. 278 (2022) 125521, https://doi.org/10.1016/J.MATCHEMPHYS.2021.125521.

[78] H.L. Wang, J.M. Han, AFM study of the morphologic change of HDPE surface photografted with glycidyl methacrylate, J. Colloid Interface Sci. 333 (2009) 171–179, https://doi.org/10.1016/J.JCIS.2009.01.023.

[79] F.-H. Chen, J.-L. Her, S. Mondal, M.-N. Hung, T.-M. Pan, Impact of Ti doping in Sm2O3 dielectric on electrical characteristics of a-InGaZnO thin-film transistors, Appl. Phys. Lett. 102 (2013), https://doi.org/10.1063/1.4807014.

[80] R. Pal, Non-Newtonian behaviour of suspensions and emulsions: review of different mechanisms, Adv. Colloid Interf. Sci. 333 (2024) 103299, https://doi.org/10.1016/J.CIS.2024.103299.

[81] Q. Zhang, J. Liu, G. Zhang, Y. Li, N. Hu, J. Yang, Y. Yang, S. Qu, Q. Kan, G. Kang, Poroelastic fracture of polyacrylamide hydrogels: enhanced crack tip swelling driven by chain scission, J. Mech. Phys. Solids 194 (2025) 105954, https://doi.org/10.1016/J.JMPS.2024.105954.

[82] H. Wang, X. Qin, Y. Feng, B. Huang, X. Zou, J. Quan, P. Lan, L. Lan, Preparation of high-performance waterborne acrylic-based adhesive for soft porcelain veneer molding, Mater. Today Commun. 46 (2025) 112869, https://doi.org/10.1016/J.MTCOMM.2025.112869.

[83] N.R. Singha, M. Mahapatra, M. Karmakar, A. Dutta, H. Mondal, P. K. Chattopadhyay, Synthesis of guar gum- g -(acrylic acid- co -acrylamide- co −3-acrylamido propanoic acid) IPN via in situ attachment of acrylamido propanoic acid for analyzing superadsorption mechanism of Pb (<scp>ii</scp>)/cd (<scp>ii</scp>)/cu (<scp>ii</scp>)/MB/MV, Polym. Chem. 8 (2017) 6750–6777, https://doi.org/10.1039/C7PY01564J.

[84] H.A.Z. Sabek, A.M.M. Alazaly, D. Salah, H.S. Abdel-Samad, M.A. Ismail, A. A. Abdel-Shafi, Photophysical properties and fluorosolvatochromism of D–π–a thiophene based derivatives, RSC Adv. 10 (2020) 43459–43471, https://doi.org/10.1039/D0RA08433F.

[85] G.-J. Zhao, K.-L. Han, Hydrogen bonding in the electronic excited state, Acc. Chem. Res. 45 (2012) 404–413, https://doi.org/10.1021/ar200135h.

[86] R.-H. Chien, C.-T. Lai, J.-L. Hong, Hydrogen bonds and enhanced aggregation emission of organic and polymeric fluorophores with alternative Fluorene and Naphthol units, J. Phys. Chem. C 115 (2011) 12358–12366, https://doi.org/10.1021/jp203261s.

[87] Y. Zhao, S. Sun, Adhesive and conductive hydrogels based on poly(acrylic acid) composites for application as flexible biosensors, Colloids Surf. A Physicochem. Eng. Asp. 698 (2024) 134575, https://doi.org/10.1016/J.COLSURFA.2024.134575.

[88] Q. He, Y. Cheng, Y. Deng, F. Wen, Y. Lai, H. Li, Conductive hydrogel for flexible bioelectronic device: current Progress and future perspective, Adv. Funct. Mater. 34 (2024), https://doi.org/10.1002/adfm.202308974.

[89] H. Maleki-Ghaleh, E. Moradpur-Tari, M. Shakiba, J. Paczesny, P.K. Hurley, M. H. Siadati, L. Ansari, F. Gity, Electronic structure of rare-earth erbium-doped platinum diselenide: a density functional theory study, J. Phys. Chem. Solids 190 (2024) 112004, https://doi.org/10.1016/J.JPCS.2024.112004.

[90] Y. Zhang, M. Dai, Z. Yuan, Methods for the detection of reactive oxygen species, Anal. Methods 10 (2018) 4625–4638, https://doi.org/10.1039/C8AY01339J.

[91] D. Yu, Y. Zha, Z. Zhong, Y. Ruan, Z. Li, L. Sun, S. Hou, Improved detection of reactive oxygen species by DCFH-DA: new insight into self-amplification of fluorescence signal by light irradiation, Sensors Actuators B Chem. 339 (2021) 129878, https://doi.org/10.1016/J.SNB.2021.129878.